

**Connectivity analysis of functional MRI data in the latent neuronal space: Applications in science and medicine**

by

Karthik Ramakrishnan Sreenivasan

A thesis submitted to the Graduate Faculty of  
Auburn University  
in partial fulfillment of the  
requirements for the Degree of  
Master of Science

Auburn, Alabama  
May 4, 2014

Keywords: Functional MRI, Blind deconvolution, Homomorphic filtering, Cubature Kalman Filter, Effective connectivity, Granger Causality

Copyright 2014 by Karthik Ramakrishnan Sreenivasan

Approved by

Gopikrishna Deshpande, Chair, Assistant Professor, Electrical & Computer Engineering  
Thomas S Denney, Director, Auburn University MRI Research Center  
Jennifer L Robinson, Assistant Professor, Department of Psychology

## Abstract

Since the inception of functional magnetic resonance imaging (fMRI) there has been a steady growth in the number of studies utilizing this non-invasive method to gain insights into the brain function in both healthy and clinical populations. In this thesis we address two key issues associated with fMRI data analysis arising due to the fact the fMRI signal is considered to be the convolution of the hemodynamic response function (HRF) and a latent neuronal response and hence is not a direct measure of the neuronal activity. First, in order to deconvolve voxel-specific HRF and recover the latent neuronal response, highly parameterized blind deconvolution models have been recently proposed. In chapter-2, we investigate whether these models are susceptible to over-fitting by proposing a non-parametric method to perform blind hemodynamic deconvolution. We also compare the performance of our method with an already existing parametric method using both simulations and experimental data. We tested the hypothesis that if the performance of these two methods were similar, then we can conclude that the parametric models are probably not susceptible to over-fitting. The results of the both simulations and experimental data supported our hypothesis, and we found that the neuronal responses were estimated effectively by both these methods and their results were very similar. The second issue is related to the use of raw fMRI data in effective connectivity (EC) analysis using Granger Causality. Non-neuronal spatial variability of the HRF has a confounding effect on the inferences that one could obtain from EC analysis using raw fMRI data. Therefore in chapter-3 we describe a novel EC model which can be used to perform directional connectivity analysis using latent

neuronal variables (as opposed to raw fMRI data) obtained by blind hemodynamic deconvolution methods described in the previous chapter. In chapter-4, we demonstrate the utility of the proposed EC model in a diverse set of fMRI studies.

## Acknowledgments

I would like to thank many people who have been very helpful in successful completion of my thesis. First, I would like to thank my advisor Dr. Gopikrishna Deshpande for his guidance, support and advice throughout the entire course of my Master's program. He helped me develop as a researcher and also become a much better human being. He motivated me, trusted me and helped me get past the difficult phases during the course of my thesis work. It was an honor working with Dr. Gopikrishna Deshpande and I express my deepest gratitude to him for his guidance, support and understanding.

I would like to thank my committee members Dr. Thomas Denney and Dr. Jennifer Robison who graciously agreed to be a part of my Master's thesis committee. I would like to express my appreciation to them for their time and their very helpful comments, advice and suggestions.

I will not be able to forget the help of my friends at the AU MRI center. Everyone here was very helpful and are a great bunch of people to be around. Especially two members of my research group Pruthviraj Kyathanahally and Hao Jia who have been of great help since the beginning of my thesis work. Pruthvi was always very helpful and supportive and his positive vibe always kept me motivated and happy. Hao was always there to help me in my projects with very useful and thoughtful points and comments.

I would also like to express my appreciation and gratitude to all my co-authors who have

contributed to the collaborative work that is a part of my thesis. I would like to acknowledge the contributions of Lauren Libero, Hrishikesh Deshpande, Dr. Rajesh Kana, Dr. Merida Grant, David White, Jennifer Hadley, Nathan Hutcheson, Dr. Richard Shelton, Muriah Wheelock, Dr. Kimberly Wood, Dr. Lawrence Ver Hoef, Dr. David Knight, Dr. Mark S. Bolding, Dr. Adrienne Lahti, Mina Hanna, Dr. Simon Lacey, Dr. Randall Stilla, Dr. Krish Sathian, Dr. Sarina Iwabuchi, Dr. Peter Liddle and Dr. Lena Palaniyappan. I would also like to thank them for giving me permission to use a one page summary of our collaborative work in my thesis.

Finally I would like to express my deepest thanks and gratitude to my parents and my sister. I cannot express in words how thankful I am to my parents Sreenivasan Janakiram and Jayashri, without their never ending love and support, I could have never been in the place I am at this very moment. My sister Swathi has always been very supportive and always found a way to cheer me up whenever my spirits were low. I would also like to thank Murali Ramachandran and Lakshmi (my uncle and aunt) and my cousins Arvind and Keerthi for their love and support during the course of my Master's program. Finally I would like to thank all my relatives and friends who have inspired me and been there for me when I needed them. Thank you.

## Table of Contents

Abstract .....	ii
Acknowledgments.....	iv
List of Tables .....	x
List of Figures.....	xi
Chapter 1 Introduction .....	1
1.1 Magnetic resonance imaging (MRI).....	1
1.2 Functional magnetic resonance imaging (fMRI).....	2
1.3 Connectivity analysis.....	3
1.4 Thesis organization.....	5
Chapter 2 Non-Parametric Blind Hemodynamic Deconvolution of fMRI using Homomorphic Filtering .....	6
2.1 Introduction.....	7
2.2 Materials and Methods.....	13
2.2.1 Non-Parametric Deconvolution Model.....	13
2.2.2 Parametric Deconvolution Model.....	17
2.2.3 Simulations .....	19
2.2.4 Experimental Data .....	22
2.3 Results.....	22
2.3.1 Simulations .....	22

2.3.2 Experimental Data .....	24
2.4 Discussion.....	25
Chapter 3 Effective Connectivity Model .....	27
3.1 Introduction.....	27
3.2 Connectivity model.....	28
3.2.1 Blind deconvolution model.....	28
3.2.2 Static MVAR model .....	30
3.2.3 Dynamic MVAR model.....	30
3.3 Connectivity Analysis.....	31
Chapter 4 Applications of the granger causality based effective connectivity model.....	33
4.1 Identification of neural connectivity signatures of autism using machine learning ....	33
4.1.1 Introduction.....	33
4.1.2 Materials and Methods.....	34
4.1.3 Results.....	35
4.1.4 Discussion .....	37
4.2 A Framework for Causal Connectivity Analysis of fMRI in Patient Populations: An application to Major Depression and Early Life stress .....	38
4.2.1 Introduction.....	38
4.2.2 Materials and Methods.....	39
4.2.3 Results.....	41
4.2.4 Discussion .....	43
4.3 Effective connectivity reveals learning-related changes in the emotional response to a threat .....	43
4.3.1 Introduction.....	43
4.3.2 Materials and Methods.....	44

4.3.3 Results.....	45
4.3.4 Discussion.....	47
4.4 Effective connectivity analysis of the memory network in schizophrenia before and after antipsychotic medication.....	47
4.4.1 Introduction.....	48
4.4.2 Materials and Methods.....	49
4.4.3 Results.....	51
4.4.4 Discussion.....	52
4.5 Effective connectivity analysis of visual-motor network in patients with schizophrenia.....	52
4.5.1 Introduction.....	53
4.5.2 Materials and Methods.....	53
4.5.3 Results.....	55
4.5.4 Discussion.....	56
4.6 Spatial imagery in haptic shape perception.....	57
4.6.1 Introduction.....	57
4.6.2 Materials and Methods.....	57
4.6.3 Results.....	59
4.6.4 Discussion.....	63
4.7 Effective connectivity among three large-scale networks in schizophrenia and bipolar disorder with psychosis.....	63
4.7.1 Introduction.....	64
4.7.2 Materials and Methods.....	64
4.7.3 Results.....	65
4.7.4 Discussion.....	66

Chapter 5 Conclusion.....	68
Bibliography .....	71

## List of Tables

Table 4.1 .....	37
-----------------	----

## List of Figures

Figure 2.1 .....	11
Figure 2.2 .....	15
Figure 2.3 .....	17
Figure 2.4 .....	19
Figure 2.5 .....	20
Figure 2.6 .....	23
Figure 2.7 .....	23
Figure 2.8 .....	25
Figure 3.1 .....	31
Figure 3.2 .....	32
Figure 4.1 .....	35
Figure 4.2 .....	36
Figure 4.3 .....	36
Figure 4.4 .....	40
Figure 4.5 .....	41
Figure 4.6 .....	41
Figure 4.7 .....	42
Figure 4.8 .....	42
Figure 4.9 .....	45

Figure 4.10 .....	46
Figure 4.11 .....	46
Figure 4.12 .....	50
Figure 4.13 .....	51
Figure 4.14 .....	51
Figure 4.15 .....	54
Figure 4.16 .....	55
Figure 4.17 .....	56
Figure 4.18 .....	59
Figure 4.19 .....	60
Figure 4.20 .....	61
Figure 4.21 .....	62
Figure 4.22 .....	66

## **Chapter 1 Introduction**

The brain is the least understood and most intriguing organ in the whole body. For a long time researchers have strived to understand the complex structure of the brain and how it processes information relating to various phenomenon like cognition, emotion, memory, etc. However, with the recent advent of magnetic resonance imaging (MRI) and functional MRI (fMRI) several studies have been conducted which helped to answer the vital questions related to the functional and structural organization of the brain.

### **1.1 Magnetic resonance imaging (MRI)**

MRI is a non-invasive medical imaging technique that has found wide and prevalent use in the fields of radiology, clinical diagnostics and in research. This technique uses a strong magnetic field in conjunction with radio waves to get images of the different structures and organs inside the body. These images are obtained by making use of the nuclear magnetic resonance (NMR) [1, 2] property of hydrogen nuclei which are available in abundance in biological tissues. The MRI scanner has a set of electromagnetic coils, gradient coils and radio frequency coils which can be considered as its three main components. The electro-magnetic coils generate a strong static magnetic field and when a person lies in the scanner the protons in the body aligns itself to the direction of the magnetic field. The gradient coils are used to generate a gradient magnetic field which is used to select the precise location of imaging in the body. Then the RF coil transfers energy to the body which is absorbed by these protons and jumps from lower energy level to higher

energy level resulting in a state of precession in the transverse direction. When the RF pulse is turned off the protons release the energy and return to the original state realigning to the static magnetic field. The energy that is released by the protons is the MR signal and this is recorded by the coils to obtain the raw data matrix. We can use the gradients in different direction to obtain the data for 2D images or 3D volumes. Then by using Fourier analysis techniques the spatial information can be recovered from obtained MR signal to get the image of the region of the body that has been scanned. The MR signal recorded is not static and changes over time. This change in signal is called as relaxation and can be classified into T1 and T2 relaxations (for detailed information about T1 and T2 relaxation reader is referred to [3]). These relaxation times are different for protons in the different tissues in the body, thus by using different parameters for scanning purposes, contrast can be created between the different biological tissues which will be helpful in distinguishing interested tissues more clearly and from surrounding area. This property of contrast manipulation leads to MR imaging giving more detailed diagnostic information about the organ being scanned when compared to other medical imaging techniques like computed tomography (CT) or X-rays.

## **1.2 Functional magnetic resonance imaging (fMRI)**

fMRI is a technique which measures the changes in the blood oxygenation levels (blood oxygenation level dependent (BOLD) signal) and gives us an indirect measure of the neuronal activity in the brain [4]. Brain requires oxygen to metabolize glucose (supplied by blood) and provide energy, like any other organ in the body. This oxygen is supplied to the brain by a component in blood called hemoglobin whose magnetic properties change with its oxygen content [5]. Oxygenated hemoglobin (HB) is diamagnetic while the deoxygenated hemoglobin (dHB) is paramagnetic. As a result, dHB content (in blood) causes a change in susceptibility of the blood

and this change in susceptibility leads to a reduction of the MR signal in that region. Thus when the neuron fires, the blood flow increases bringing in more glucose and oxygen by means of HB replacing the dHB. Initially due to the presence of dHB in the region its paramagnetic properties cause the MR signal to reduce and thus when it is displaced by diamagnetic HB, the increase in the flow of blood in the vessels leads to an inherent increase in MR signal [6]. Thus it can be observed that the neural activity and blood flow are coupled, i.e the firing of neurons causes an increase in blood flow in that locality. This increase brings in more HB leading to a decrease in content of dHB causing a subsequent increase in the MR signal. This way the fMRI technique uses the dependency of brain on oxygen and measures blood flow to give us the picture of activity in the brain. The fMRI technique has a very good spatial resolution when compared to other imaging techniques. In addition to this, since fMRI is non-invasive and does not involve radiation, contrast agents or surgery it has developed into a dominant and essential tool in for studying the functional organization of the brain for both research and clinical purposes. Specifically there has been an explosion in the number of studies that have used fMRI to study the connectivity between different regions of the brain.

### **1.3 Connectivity analysis**

The neuronal connectivity networks have been attracting the interest of many researchers from a very long time, and with the help of fMRI there have been numerous studies to understand brain functioning in various simple and complicated motor, cognitive and behavioral tasks. In the early nineties, these studies mainly focused on spatial localization of the functioning of the brain [7]. According to these studies the brain had certain specialized regions for each function and that the functionality corresponding to these tasks or functions was associated with these distinct spatially localized regions. A great deal of progress was made based on this model, which provided

remarkable information related to the working of the brain. However this model was not very adept in explaining the higher level functions which lead to the development of another model of brain functionality which was the distributed information processing model. This model was based on the principle that brain function is not only restricted to specific spatially localized networks but also requires a connection between networks for exchange of information. Essentially this model included the spatial localization model, postulating that simple functions are processed in specific localized networks and a link between these networks contributed to more complex and higher level processes.

The interactions between these regions can be causal relationship i.e. information flow from one region to another where one region causes activity in the other [8, 9, 10] or simultaneous activity in different brain regions which can be caused by the network synchronizations [11]. Friston referred to these two types of relationships (simultaneous and causal) between the different regions of the brain obtained from fMRI data as functional connectivity (FC) and effective connectivity (EC) [12] respectively. Several studies have been conducted since then to study the FC between different regions of the brain, primarily using correlation coefficient, in resting state [13] and also in task based studies [14]. Whereas EC has been extensively investigated in task based studies [15, 16, 17, 18] and comparatively lesser resting state studies [19, 20, 21].

Basically majority of the FC analyses use the concept of correlation or independent component analysis to study the synchronized connectivities in the brain. While there are a lot of methods in EC analyses like dynamic causal modeling (DCM) [18], structural equation modeling (SEM) [22] and Granger causality analysis [15, 17, 23, 24, 25]. The reason for utilization of different methods for EC analyses arises from the fact that the concept of causal influence is diverse with a lot of

different interpretations and is not as straightforward as the concept of synchronization in FC analyses.

#### **1.4 Thesis organization**

One of the major issues these methods (EC methods) face however is the fact that the fMRI signal is an indirect measure of the neuronal activity. It is considered to be given by a convolution of the neuronal activity and the canonical HRF, and the non-neuronal spatial variability of the HRF [26] confounds the ability to infer causal connections between the latent neuronal variables when these methods use raw fMRI data for connectivity analysis [27, 28]. Subsequently deconvolving the HRF from the fMRI response prior to EC analysis was proposed as a solution [28, 29, 30, 31]. The second chapter of this thesis we discuss about the concerns related to over-fitting problem of the already existing deconvolution methods that have been implemented to eliminate this non-neuronal variability of the HRF. The main emphasis of chapter-2 is the non-parametric method for blind deconvolution we have proposed, and comparison of its performance with an already existing parametric model of deconvolution [32] to investigate the skepticism related to highly parameterized models suffering from the problem of overfitting. In the third chapter we discussed a novel connectivity model based on granger causality which performs effective connectivity analysis on the latent neuronal variables obtained by blind deconvolution using the cubature kalman filter technique [32] and not the raw fMRI data, subsequently eliminating the effect of HRF variability on the connectivity measures. In chapter-4 we demonstrated the utility of the connectivity model discussed in chapter-3 by applying it to diverse set of human fMRI data to investigate the effective connectivity network patterns in the human brain. Finally the chapter-5 concludes the findings of this thesis.

## **Chapter 2 Non-Parametric Blind Hemodynamic Deconvolution of fMRI using Homomorphic Filtering**

Authors: Karthik Sreenivasan<sup>1</sup>, Martin Havlicek<sup>2</sup>, Gopikrishna Deshpande<sup>1,3</sup>.

<sup>1</sup> AU MRI Research Center, Department of Electrical and Computer Engineering, Auburn University, Auburn, AL.

<sup>2</sup> Department of Cognitive Neuroscience, Maastricht University, Maastricht, Limburg, Netherlands.

<sup>3</sup> Department of Psychology, Auburn University, Auburn, AL.

Contributions: conceived and designed the project: GD. Implementing the model: KS, guided by GD and MH. Wrote the paper: KS, GD, MH.

Functional MRI (fMRI) is an indirect measure neural activity which is modeled as a convolution of the latent neuronal response and the hemodynamic response function (HRF). Since the sources of HRF variability can be non-neural in nature, the measured fMRI signal does not faithfully represent underlying neural activity. Therefore, it is advantageous to deconvolve the HRF from the fMRI signal. However, since both latent neural activity and the voxel-specific HRF is unknown, the deconvolution must be blind. Existing blind deconvolution approaches employ highly parameterized models, and it is unclear whether these models have an over fitting problem. In order to address these issues, we (1) present a non-parametric blind deconvolution method based on homomorphic filtering to obtain the latent neuronal response from the fMRI signal and, (2) compare our approach to the best performing existing parametric model based on the estimation of the biophysical hemodynamic model using the Cubature Kalman Filter/Smother. We hypothesized that if the results from non-parametric deconvolution closely resembled that obtained

from parametric deconvolution, then the problem of over fitting during estimation in highly parameterized deconvolution models of fMRI can be ignored. Both simulations and experimental results demonstrate support for our hypothesis since the estimated latent neural response from both parametric and non-parametric methods were highly correlated. Further simulations showed that both methods were effective in recovering the simulated ground truth.

## **2.1 Introduction**

Over the last two decades, functional magnetic resonance imaging (fMRI) has been used to investigate brain regions involved in sensory, motor and cognitive functions. fMRI measures hemodynamic responses secondary to neural activity, and hence is an indirect measure of the latter. Mathematically, the fMRI signal is modeled as a convolution of the hemodynamic response function (HRF) and unmeasured latent neuronal variables which are driven by the external stimulus in task studies [33]. Consequently, the HRF is the impulse response which governs the relationship between neural activity and the measured fMRI signal. The shape of HRF has been modeled using the nonlinear hemodynamic model [34, 35, 36] [37, 38] which essentially models the dynamic changes in the volume and flow of blood caused by neural activity and corresponding changes in the functional MR signal.

The fact that the fMRI signal is a filtered version of neural activity raises many issues while using it as a tool for understanding brain function. For example, it has been shown that the HRF varies across different subjects and also between different regions of the brain [26], which causes non-neuronal variability in the fMRI response [39]. This variability could confound results obtained from raw fMRI time series. One such example is the study of effective connectivity between the different regions of the brain. The studies investigating effective connectivity (causal influence of

one brain region over another) in the brain have used different approaches based on exploratory techniques, which do not make any assumptions about the connection architecture, such as Granger causality [15, 17, 19, 23, 24, 25, 40, 41, 42, 43] [44, 45, 46, 47], and confirmatory approaches such as Dynamic Causal Modeling [18, 48, 49, 50, 51] which make prior assumptions about the underlying connectional architecture. However, given the fact that variance in the fMRI signal could be influenced by non-neuronal sources of variability in the HRF, studies have shown that the causal metrics obtained from raw fMRI time series can be confounded by this factor [27, 28]. Therefore deconvolving out the HRF from the fMRI signal and modeling interactions between brain regions in the latent neuronal space as in DCM, could be advantageous in this emerging field of causal connectivity analysis.

Deconvolving the HRF from the fMRI signal is an ill-posed problem since both the exact shape of the HRF and the latent neural variable input are unknown. What is measured is only the output of the convolution, i.e. the fMRI signal. Activation studies employing the general linear model have circumvented this problem by using a single canonical HRF in the model. This is less likely to be a problem since such univariate models are not very sensitive to the temporal information in the data and whatever mismatch that exists between the canonical and actual HRFs can be modeled by using time and dispersion derivatives in the general linear model (GLM). However, multivariate effective connectivity models are designed to investigate this temporal information, and hence, cannot use a canonical HRF in deconvolution. This calls for the deconvolution of the fMRI signal wherein the latent neural variables as well as the voxel-specific HRF are jointly estimated based on the output of the system, i.e. the observed fMRI signal.

Quite a few deconvolution methods have proposed in the past which can be divided into primary into three types of approaches: (1) Semi-blind parametric approaches which make definitive

assumptions about the shape of the HRF or the neural activity as defined by an underlying parametric model, (2) Semi-blind non-parametric approaches which do not make assumptions about the HRF, but at the same time, do not jointly estimate both the HRF and the latent neural variables, and (3) Blind parametric approaches which do not make restrictive assumptions about the HRF or latent neural variables, but rather use physiologically plausible priors on parameters controlling the HRF during estimation, and importantly, jointly estimate the HRF and latent neural variables. Examples for the first case include the method proposed by Bush *et al* [52] that assumes the shape of the HRF and uses non-linear regression modeling approach to deconvolve the fMRI signal. Gaudes and colleagues proposed two deconvolution methods [53, 54] which performed deconvolution of the hemodynamic response using a ridge-regression algorithm and sparse regression techniques, respectively. The performance of ridge-regression algorithm was evaluated on experimental task data while the performance of the sparse regression technique was evaluated using simulated data as well as experimental task data. Another similar method which uses an iterative estimation algorithm for deconvolving the fMRI signal was introduced by Hernandez-Garcia *et al* [55]. This scheme implemented a method of majorization-minimization of a cost function for estimation. The performance of the algorithm was tested using simulated data and it was also applied to experimental data using both block and event-related designs. Recently Karahanoğlu *et al* [56] proposed a method called “total activation” which implemented a variational framework. A cost function was formulated by including spatial and temporal regularization terms which were solved using iterative shrinkage algorithms. This method was validated using simulated data and was also applied to experimental resting state and task data. Wu *et al* [57] proposed wherein they considered resting state fMRI as a spontaneous event related process and extracted the HRFs, assuming that they are canonical, and used them in a Weiner filter

based deconvolution model to obtain the latent neural variables. Khalidov *et al* [58] implemented a sparse search technique in a wavelet basis which was modified based on hemodynamic properties called as the Activelet domain. They modeled the HRF based on a linearized set of differential equations as in Friston *et al* [36]. This approach was validated and its feasibility was shown using both simulated as well as experimental data.

One of the limitations of semi-blind parametric methods described above is that the definitive assumptions they make about the HRF may not hold true since the HRF has been shown to be variable in different regions as well as different subjects [26]. Despite showing very good results with simulated and simple experimental task data, semi-blind parametric approaches have not yet been demonstrated to be able to recover the HRF as well as latent neural variables in the presence of HRF variability of non-neural origin.

Few studies use semi-blind non-parametric approaches. One example is the study by Wink *et al* [59] wherein they adopted a data driven method using Fourier-wavelet regularized deconvolution technique which is a combination of frequency domain deconvolution, frequency domain regularization and wavelet domain regularization. This extraction algorithm was validated using both simulated and experimental data. Another semi-blind non-parametric approach was proposed by Glover [60] where in the HRF was experimentally estimated using a short-stimulus calibration trial and then subsequently used in a Weiner filter for deconvolution of the hemodynamic response from fMRI data. The fact that neural latent variables were not jointly estimated with the HRF in these semi-blind non-parametric approaches raises the possibility that observed variance in the fMRI signal could be wholly attributed to the variance in the HRF without taking into account the possibility that the external stimulus might induce variances in the latent neural variables of interest.

Blind parametric approaches model the complex physiological process that describes the relationship between neural activity and blood flow using highly parameterized mathematical models (Example: the hemodynamic model [36, 37, 38]) and jointly estimate these models and underlying latent neural variables driving them. Figure 2.1 shows a schematic of the neural model, hemodynamic model and the measurement model (are illustrated based on figure 1 from [61]). In this model the external input  $u(t)$  drives the hidden neuronal variable  $n(t)$  which in turn drives flow ( $f(t)$ ) through inducing signal  $s(t)$ . The flow variable drives corresponding changes in blood volume

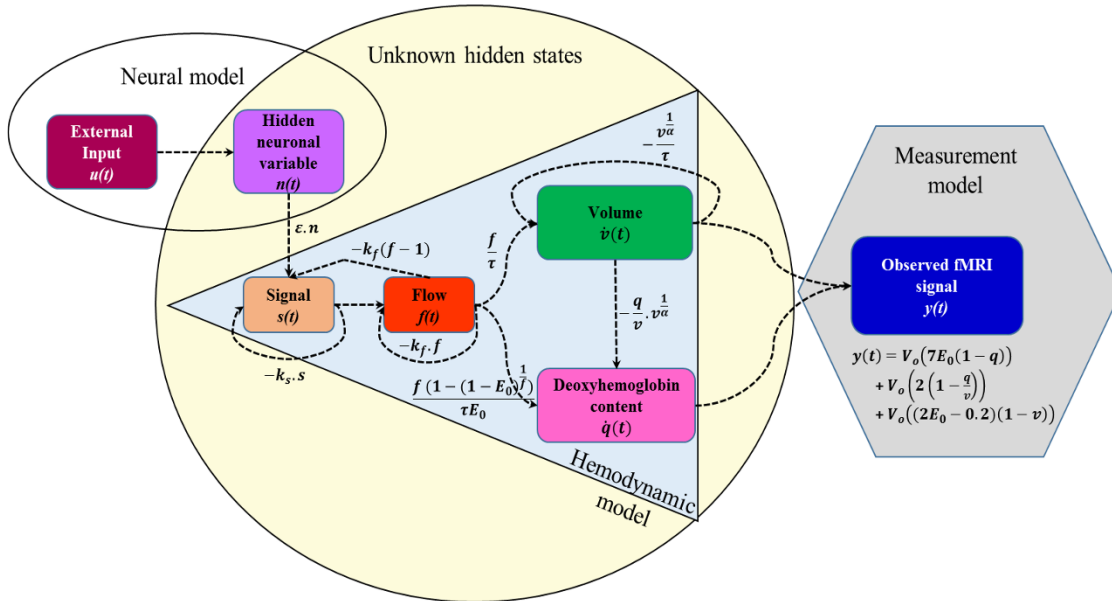


**Figure 2.1:** The hemodynamic model, neural model and the measurement model. The variables  $\varepsilon$  is the efficacy with which the latent neuronal input ( $n(t)$ ),  $k_s$  is the parameter indicating signal ( $s(t)$ ) decay,  $k_f$  is the parameter representing the autoregulatory feedback of blood flow ( $f(t)$ ),  $\tau$  is the transit time,  $\alpha$  is the Grubbs exponent,  $v$  represents the volume of blood flow,  $q$  represents deoxyhemoglobin content,  $E_0$  is the net oxygen extraction by the capillary bed and  $V_0$  is the resting blood volume fraction.

$\dot{v}(t)$  and deoxyhemoglobin content  $\dot{q}(t)$  of blood to give rise to the observed fMRI signal  $y(t)$ . In the figure 2.1 the parameter  $\varepsilon$  is the efficacy with which the latent neuronal variable affects the flow inducing signal ( $s(t)$ ),  $k_s$  is the parameter indicating signal ( $s(t)$ ) decay, and  $k_f$  is the parameter representing the autoregulatory feedback of blood flow ( $f(t)$ ). The variable  $\tau$  represents the transit

time which is the mean time taken to traverse the venous compartment,  $\alpha$  is the Grubbs exponent which models the outflow of volume from the venous compartment,  $E_0$  is the net oxygen extraction by the capillary bed,  $v$  represents the volume of blood flow,  $q$  represents deoxyhemoglobin content and  $V_0$  is the resting blood volume fraction (for detailed explanation, the reader is referred to [37]). Algorithms have been developed which estimate the parameters of the bio-physical hemodynamic model in order to evaluate the voxel-specific HRF and corresponding hidden neuronal variables using different methods such as Bilinear Dynamic System (BDS) [62], modified BDS [63], the Cubature Kalman Filter/Smoothing (CKF-S) [32], Dynamic expectation maximization (DEM) [64], and local linearization filter (LLF) [65]. These methods rely on prior distributions of the parameters of the hemodynamic model based on the range of their physiological plausibility to estimate most likely estimates of the parameters which shape the HRF as well as latent neural variables. These parametric methods have been shown to perform very well in simulations [32, 64]. Further, application of effective connectivity models to fMRI data deconvolved using parametric models seems to provide neuroscientifically more reasonable brain networks than those networks obtained from raw fMRI data [28, 29, 30, 31].

Blind parametric models seem to overcome the disadvantages of semi-blind methods (which were listed above). However, in estimation of the hidden variables, the main question to be answered is whether these highly parameterized methods are susceptible to over fitting? Wink *et al* [59] raise this possibility in their report and propose a non-parametric data-driven approach for deconvolution. However, since their method is semi-blind and suffers from the disadvantage of not jointly estimating the HRF and latent neural variables, it is probably not an ideal method to compare with blind parametric approaches. Yet, such a comparison of blind parametric and non-parametric fMRI deconvolution approaches is essential in order to investigate whether highly

parameterized models are susceptible to over fitting. Therefore, in this paper, we have proposed a blind non-parametric method to perform hemodynamic deconvolution based on the concept of homomorphic filtering. This approach does not make any assumptions about the shape of the HRF and also does not use a parametric model to deconvolve the fMRI signal. Rather, this approach utilizes the fact that HRF is a predominantly low frequency response while latent neural variables have predominantly higher frequencies as compared to the HRF, and hence, are separable in the frequency domain. This concept of homomorphic filtering has been widely used for non-parametric blind deconvolution in speech signal processing in order to recover the fundamental frequency (pitch) [66], on seismic data to determine the depth of the ocean floor [67, 68], in blast vibration data to identify the impact force [69], in brain perfusion imaging to estimate the arterial input function [70], and in archival restoration through blind deconvolution of images [71].

We have compared the performance of the homomorphic filtering method with the best performing blind parametric method, i.e. the CKF method proposed by Havlicek *et al* [32], for deconvolving fMRI responses using both simulated and experimental data. Specifically, we test the hypothesis that the CKF method is not susceptible to over-fitting and hence, latent neural variables obtained from the CKF method will be significantly correlated with that obtained from the non-parametric homomorphic filtering method.

## **2.2 Materials and Methods**

### **2.2.1 Non-Parametric Deconvolution Model**

The acquired fMRI signal is considered to be a convolution between the unmeasured latent neuronal response and the HRF. As discussed earlier, the deconvolution of the HRF from the fMRI response is a complex problem because we have no information about the voxel-specific shape of

the HRF and underlying neural activity. Here we elaborate on a method for non-parametric deconvolution of the fMRI signal by using a homomorphic filtering scheme based on a specific application of homomorphic systems which was introduced by Oppenheim [72, 73]. We know that the HRF is a predominantly low frequency signal while the neuronal response is a comparatively higher frequency signal. This information is used by the proposed method of deconvolution in separating and recovery of these two components (neuronal response and HRF) from the measured fMRI signal as described below.

Let us consider the linear mathematical model which describes the measured fMRI response  $f(t)$  as a convolution of hidden neural variable  $x(t)$  and HRF  $h(t)$  as shown below

$$f(t) = x(t) * h(t) \quad (1)$$

Where “\*” denotes the convolution operation. The Fourier transform  $F(\omega)$  of the observed fMRI signal  $f(t)$  is obtained by

$$F(\omega) = X(\omega).H(\omega) \quad (2)$$

Here,  $F(\omega)$  is expressed as a product of Fourier transforms  $X(\omega)$  and  $H(\omega)$  of the neuronal signal and the HRF, respectively. The product of these Fourier transforms is then converted to a sum of their log Fourier transforms by employing a complex logarithm on both sides of Eq.2, as shown in Eq.3.

$$\log\{F(\omega)\} = \log\{X(\omega)\} + \log\{H(\omega)\} \quad (3)$$

Subsequently, an inverse Fourier transform is applied to Eq.3 in order to obtain cepstral domain representations of the signals as in Eq.4

$$\hat{f}(n) = F^{-1}\{\log\{F(\omega)\}\} = F^{-1}\{\log\{X(\omega)\}\} + F^{-1}\{\log\{H(\omega)\}\} = \hat{x}(n) + \hat{h}(n) \quad (4)$$

This procedure described above is the implementation of the complex cepstrum of a signal [74]. The complex cepstrum is defined as the inverse Fourier transform of the complex logarithm of the Fourier spectrum of a given signal. In Eq 4  $\hat{f}(n)$  is the cepstrum or quefrency domain representation of the fMRI signal  $f(t)$ . Note that the term complex is referred to the use of complex logarithm and not in relation to the input sequence, i.e. the complex cepstrum for a real sequence is also real. It is to be noted that initially, the right hand side of the Eq 1 was a convolution between the neuronal response and the HRF in the time domain and after applying the non-linear log operator, the right hand side of Eq 4 represents the summation of the neuronal response and the HRF in the cepstral domain. This is the property of the characteristic system of deconvolution which was defined by Oppenheim as the first of the three systems in the canonical form of homomorphic systems. Figure 2.2 shows a block diagram of the canonical form of the homomorphic system for deconvolution.

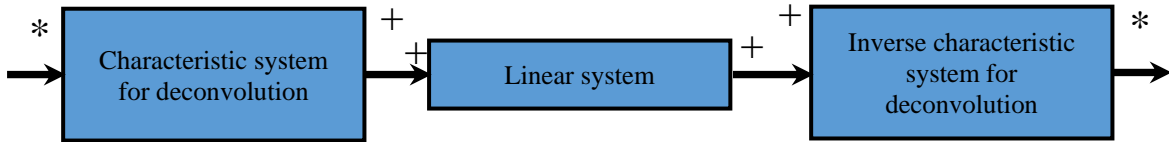


**Figure 2.2:** The homomorphic system for deconvolution

Thus, the characteristic system of deconvolution implements the concept of complex cepstrum and converts convolution between the neuronal response  $x(t)$  and the hemodynamic response  $h(t)$  in the time domain to linear sum of the cepstrum of the neuronal response  $\hat{x}(n)$  and cepstrum of the HRF  $\hat{h}(n)$  (Eqs 1-4). The complex cepstrum  $\hat{f}(n)$  of the fMRI signal is then input to a linear filter

which performs liftering operation (filtering in quefrency domain is referred to as liftering) (Eq. 5).

$$\hat{x}(n) + \hat{h}(n) \xrightarrow{\text{high pass filter}} \hat{x}(n) \quad (5)$$

This linear filter is the second of the three systems in the canonical form of homomorphic systems (Figure 2.2). Since the neuronal response and the HRF are high and low frequency signals, respectively, they occupy high and low quefrency (independent variable of the cepstrum) ranges in the cepstral domain, respectively. As a result, high pass liftering of the cepstrum  $\hat{f}(n)$  at a certain cutoff quefrency results in the separation of the cepstrum of the neuronal response  $\hat{x}(n)$  and the cepstrum of the HRF  $\hat{h}(n)$  (Eq. 5). This is then input to the third system in the canonical form of the homomorphic system of deconvolution, which is the inverse of the characteristic system and converts the neuronal response from the cepstral domain back to the time domain to give an estimate the hidden neuronal response (Eq. 6).

$$\tilde{x}(n) = F^{-1}\{\exp\{F\{\hat{x}(n)\}\}\} \quad (6)$$

Where “*exp*” denotes a complex exponential operation. Figure 2.3 shows a detailed schematic illustrating the specific implementation of the general homomorphic deconvolution system shown in figure 2.2.

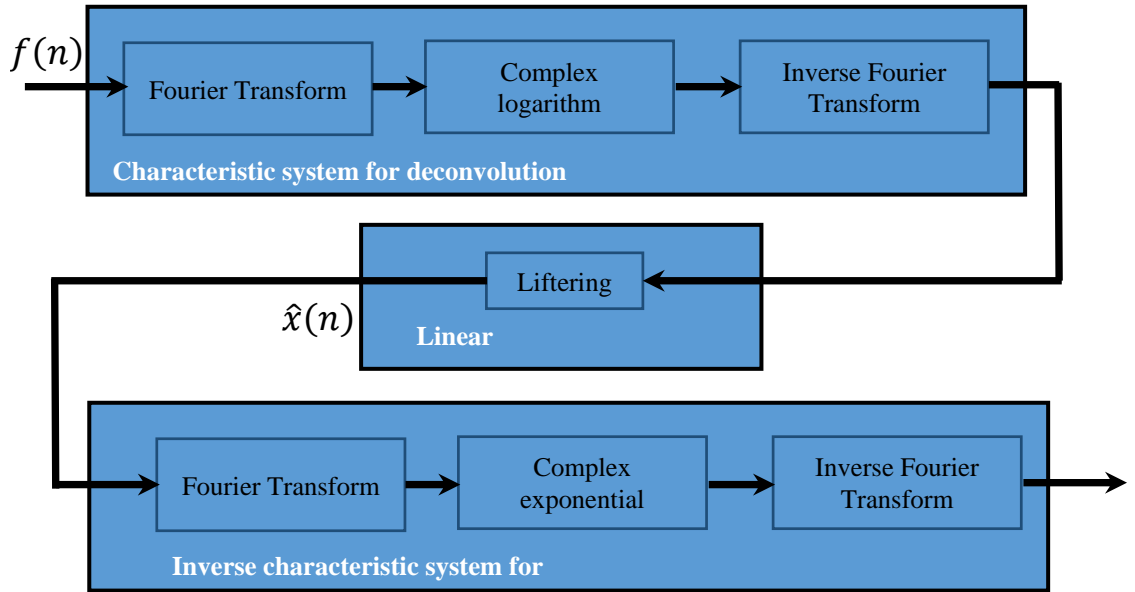


**Figure 2.3:** Schematic illustrating the specific implementation of the general homomorphic deconvolution system shown in figure 2.2

### 2.2.2 Parametric Deconvolution Model

In this paper, we have used the parametric deconvolution method based on Cubature Kalman Filters/Smoothers (CKF) [32], to recover the hidden neuronal variables and voxel-specific HRFs from simulated fMRI data. The CKF method has been shown to out-perform the deconvolution model employed in DCM as well as other blind deconvolution methods. Further, its success is attributed to the fact that it is highly parameterized for modeling every aspect of the underlying biophysics. Consequently, it is the right choice for comparison with non-parametric deconvolution to test whether high level of parameterization leads to overfitting. The method of nonlinear Kalman filtering is a very close approximation of the Bayesian filter, and uses an efficient joint estimation scheme where the parameters shaping the HRF as well as latent neural variables driving the model are combined into a single joint state vector and estimated together in a recursive manner. The dynamic joint estimation state-space model can be described as follows.

$$\tilde{\mathbf{n}}_{\tau}^v = \begin{bmatrix} n_{\tau}^v \\ i_{\tau}^v \\ p_{\tau}^v \end{bmatrix} = \begin{bmatrix} \lambda(n_{\tau-1}^v, i_{\tau-1}^v, p_{\tau-1}^v) \\ i_{\tau-1}^v \\ p_{\tau-1}^v \end{bmatrix} + \begin{bmatrix} Q_{\tau-1}^v \\ W_{\tau-1}^v \\ E_{\tau-1}^v \end{bmatrix} \quad (7)$$

Where the hidden state variables ( $n$ ), the external stimulus ( $i$ ) and the HRF parameter variables ( $p$ ) are combined together to form a single state vector. Note that the model would work fine even in the absence of the external stimulus [32].  $\lambda$  is the function linking their current states to the previous states. Here the subscript  $\tau$  indicates the continuous time and number of time series in the model is indicated by the superscript  $v$ . The Gaussian state noise vectors are represented by  $Q$ ,  $W$  and  $E$ . The observation equation, which links the state to observation variables, is as follows.

$$x_v(t) = \mathbf{m}(\tilde{\mathbf{n}}_t^v) + Z_{t-1} \quad (8)$$

Here the state and measurement variables are linked by the measurement function  $\mathbf{m}$ , the time is discretized and is represented by  $t$ , and the variable  $Z$  represents the random measurement noise with Gaussian distribution. The inputs to the model are the measured fMRI time series  $x_v(t)$  ( $v$  indicates the number of time series). As mentioned before, the experimental boxcar function i.e the exogenous input  $i$ , are optional inputs if available. Based on these inputs, the Cubature Kalman Filter performs very efficient joint recursive estimation of underlying neuronal state variables and parameters. For detailed explanation about this method, the reader is referred to [32].

### 2.2.3 Simulations

A sequence of impulses of equal amplitude convolved with a Gaussian function was generated as the hypothetical latent neural variable (figure 2.4a). This was then convolved with a canonical HRF obtained from SPM (figure 2.4b). The resultant signal (ideal fMRI signal) with TR of 1ms was down-sampled (by a factor  $M=1000$ ) to mimic a TR of 1 s to get the ideal fMRI signal (no noise). To this signal random white noise (with zero mean and standard deviation (SD) equal to half the SD of ideal fMRI signal) was added to obtain the simulated fMRI data (figure 2.4c). This was input to the homomorphic system described above wherein, the cepstral domain representation of the fMRI signal was obtained.

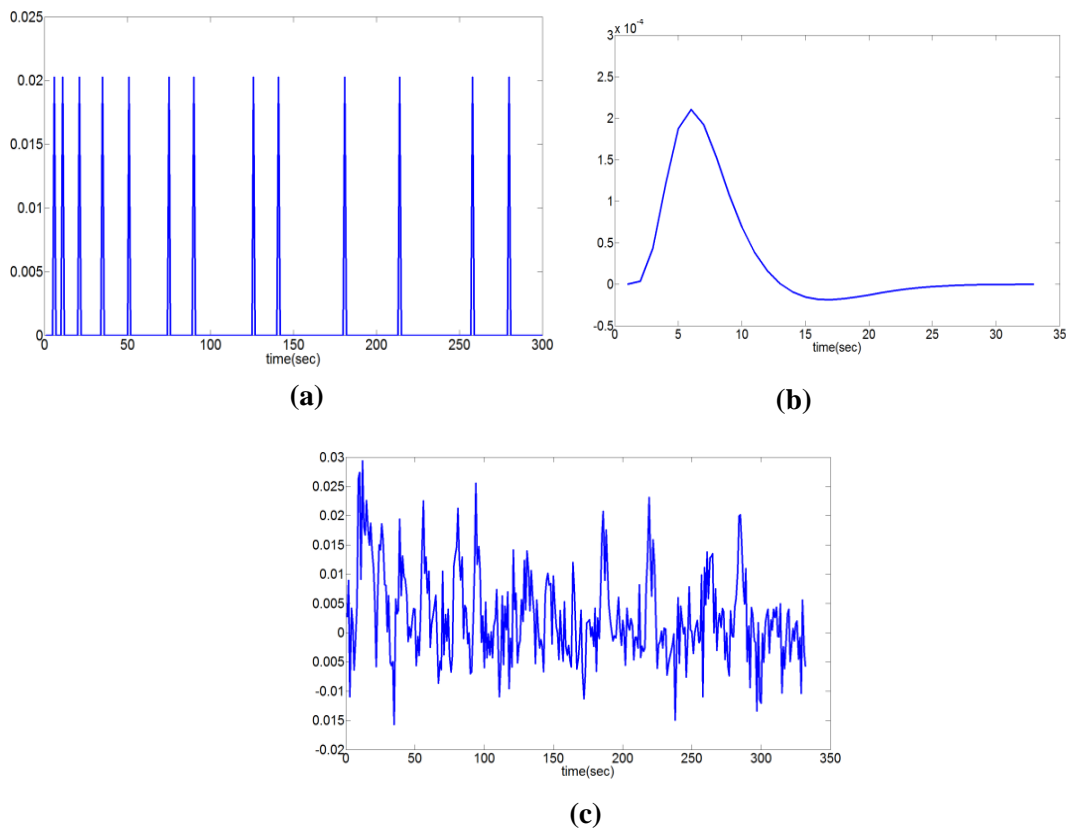


**Figure 2.4** (a) Simulated input  $x(n)$  ; (b) Simulated HRF  $h(n)$  ; (c) Hypothetical fMRI signal  $f(n)$

As stated earlier, the HRF and the latent neuronal signals have predominant energy in low and high frequencies, respectively. Therefore, based on the correspondence between quefrequency and frequency [75], the low quefrequencies of the cepstrum will have the HRF information and high quefrequencies of the cepstrum will have information on the latent neural variables. Consequently, a threshold can be defined to separate the HRF from the latent neural variables in the cepstral domain (figure 2.5).

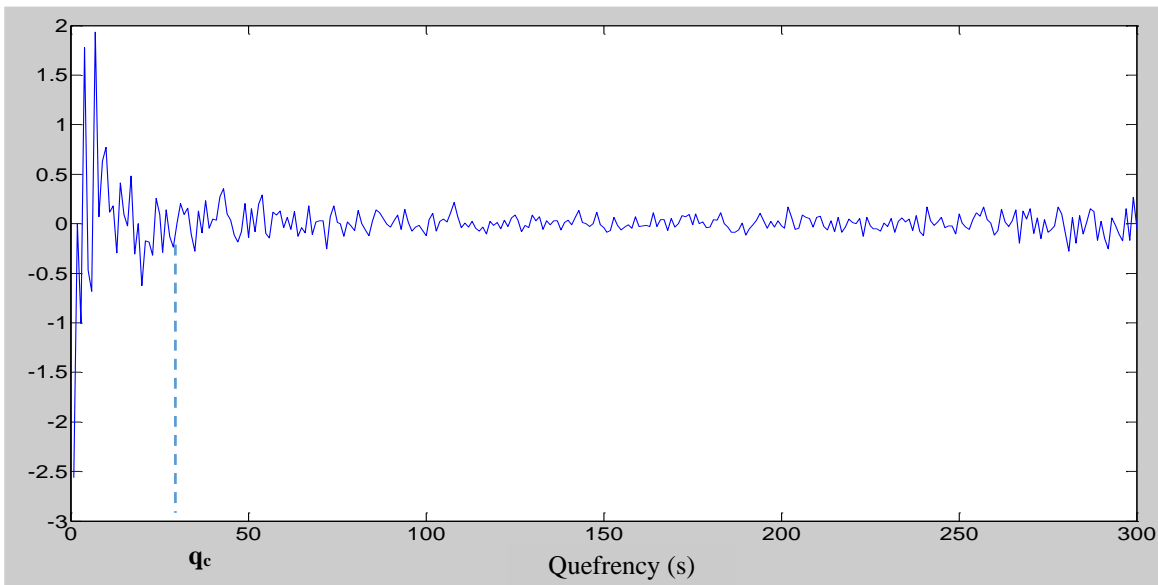


**Figure 2.5** Cepstral domain representation of simulated fMRI signal.  $q_c$  represents the threshold used to separate the cepstrums of the latent neural signal and the HRF

Therefore, we performed high pass liftering of the cepstrum obtained from simulated fMRI data at a particular cutoff quefrequency  $q_c$ . The resulting signal was passed through the inverse characteristic system (figure 2.3) to obtain the estimated latent neuronal response. We choose a threshold quefrequency by performing a grid search over the range of quefrequency values and fast Fourier transform (FFT) lengths. The length of the FFT plays an important role in the resolution of the cepstral domain. The length of the FFT was varied starting from the original length of the sequence to 10 times the length of the sequence. Thus, homomorphic filtering was performed for various quefrequency thresholds and FFT lengths and corresponding latent neuronal responses were

obtained. We then calculated the normalized maximum cross-correlation magnitude (NMCC) between the estimated and simulated latent neuronal variables. This measure can be obtained by taking the maximum absolute value of cross correlation between the two signals divided by the product of Euclidean norm of the two signals. The NMCC for two signals  $x$  and  $y$  with lengths  $a$  and  $b$  can be obtained as shown below

$$NMCC_{xy} = \frac{\max(|crosscorr(x,y)|)}{\sqrt{(\sum_{i=1}^a x(i)^2) \times (\sum_{i=1}^b y(i)^2)}} \quad (9)$$

Where “*max*” denotes maximum, and “*crosscorr*” gives the cross correlation sequence between  $x$  and  $y$ . The threshold quefrency and FFT length corresponding to the estimated latent neuronal response with the maximum NMCC was obtained and the corresponding estimated latent neuronal response was deemed to the best non-parametric estimate of the simulated neural variable. This process was repeated iteratively for every 2000 different instantiations of the additive random noise used in the simulation.

The latent neuronal variables were also estimated using the parametric CKF method from simulated fMRI data. Prior distributions of the HRF as well as other model parameters were similar to those used by Havlicek et al [32]. Similar to the non-parametric method, the simulation of fMRI data and estimation of the latent neural variables by the CKF method, were repeated 2000 times by addition of different instantiations of the random noise. In each instance, NMCC between the simulated and estimated latent neural variables were computed.

## **2.2.4 Experimental Data**

BOLD fMRI data were acquired from three healthy volunteers in a 7T scanner using a classical flashing checkerboard visual stimulation block-design paradigm. The stimulus consisted of 2 s flashing of checkerboard followed by a fixation cross for 16 s. Seventeen such trials were acquired from each subject. Data were acquired using the following scan parameters: TR=250 ms, TE=25 ms, flip angle= 30°, FOV=128 mm×128 mm, voxel size=1 mm×1 mm, slice thickness of 2 mm and with slice coverage limited to the primary visual cortex.

Following standard pre-processing and GLM analysis in SPM8, activated voxels in the primary visual cortex were identified and the mean time series from such voxels were extracted and input to both the parametric CKF model as well as the non-parametric homomorphic filter. Finally, the NMCC between the latent neural variables estimated from both methods were obtained.

## **2.3 Results**

### **2.3.1 Simulations**

Figure 2.6 shows the simulated and estimated latent neuronal variables recovered by using the homomorphic filtering method for a randomly chosen iteration. For comparison the same simulated fMRI signal was also deconvolved using the Cubature Kalman Filter (CKF) approach. Figure 2.7 shows the simulated and estimated latent neuronal variables recovered by using the CKF method for a randomly chosen iteration.

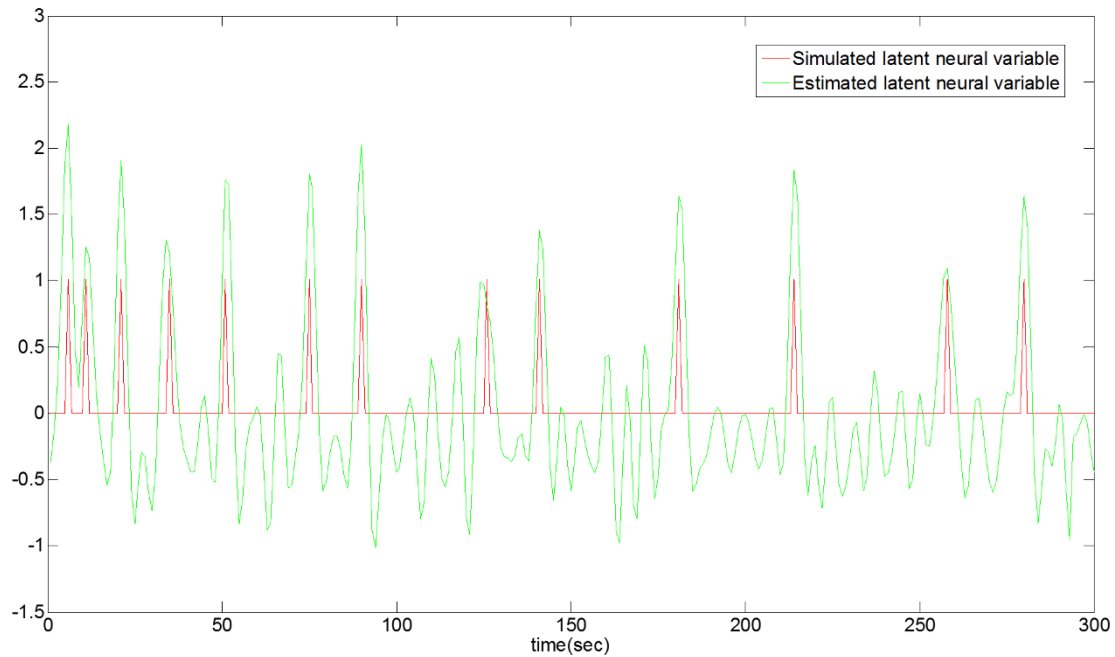


**Figure 2.6** The simulated (red) and estimated (green) latent neural variable obtained from the homomorphic deconvolution method

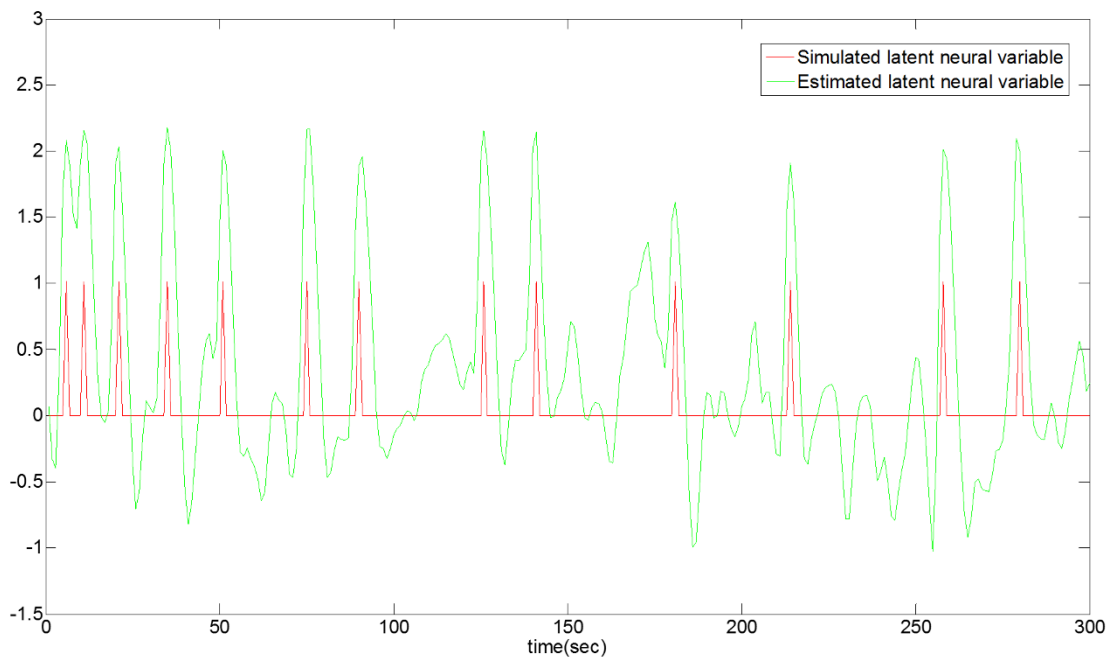


**Figure 2.7** The simulated (red) and estimated (green) latent neural variable obtained from the CKF deconvolution method

The NMCC between the simulated and estimated latent neural variables over all iterations were  $0.51 \pm 0.01$  for the parametric CKF method and  $0.53 \pm 0.02$  for the non-parametric homomorphic

method. The NMCC between the estimated latent neural variables from CKF and homomorphic methods was  $0.78 \pm 0.04$ . All three correlations were statistically significant ( $p < 0.05$ ). It is evident from these results that both methods were able to successfully recover the temporal information in the simulated latent neural variable. Further, latent neural variables estimated from both methods were highly correlated.

### **2.3.2 Experimental Data**

Figure 2.8 shows the estimated latent neural variables obtained from mean fMRI BOLD time series representing activated voxels in the primary visual cortex in three subjects, along with the timing of the external visual stimulus. It can be seen that both the CKF and homomorphic methods were able to accurately estimate the peak neural response following the external visual stimulus. Further, NMCC between estimated latent neural variables from both parametric and non-parametric blind deconvolution methods for the three subjects were 0.65, 0.56 and 0.52, respectively. All three correlations were statistically significant ( $p < 0.05$ ). These results demonstrate that latent neural variables estimated from both methods not only reflected the timing of the external stimulus, but also were highly correlated with each other.

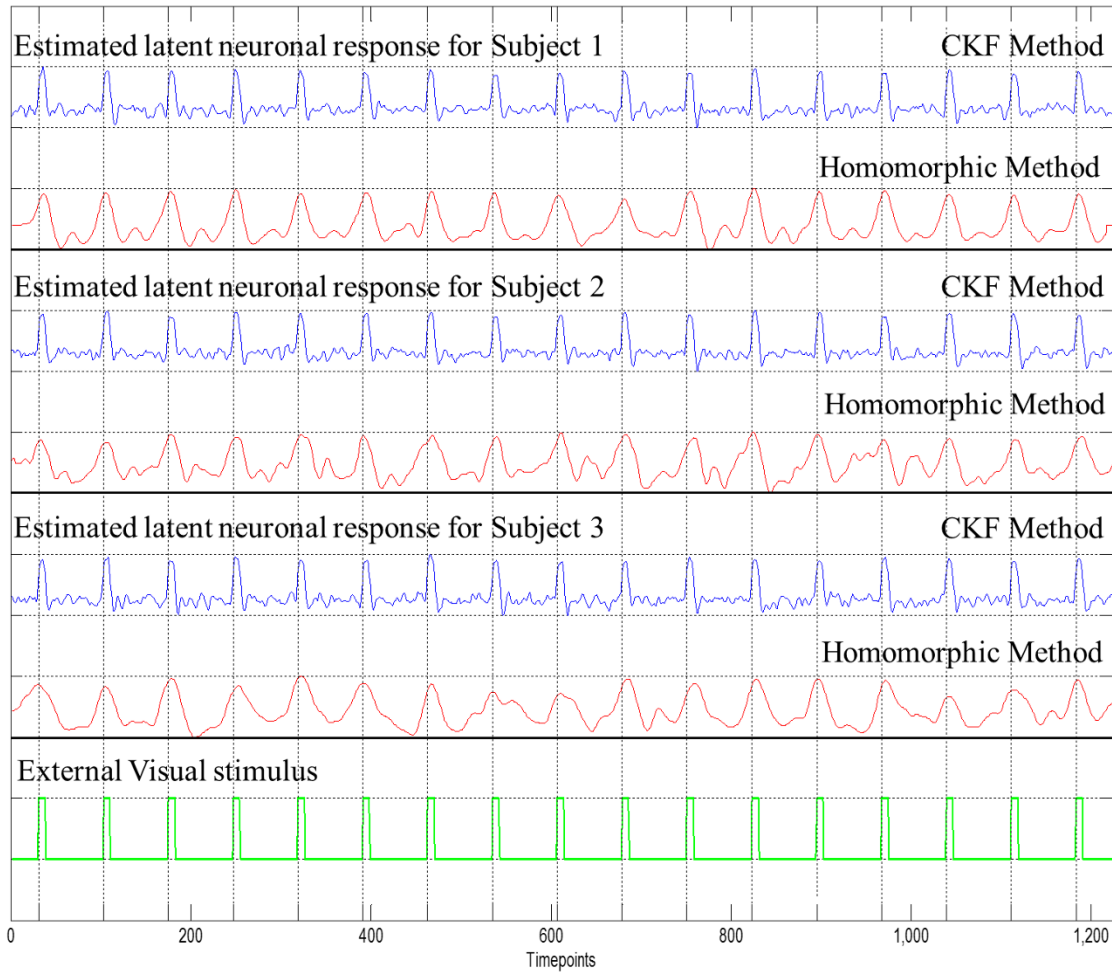


**Figure 2.8** The estimated latent neuronal variables using the CKF deconvolution method (blue) and the homomorphic deconvolution method (red) for all the three subjects along with the external visual stimulus (green).

## 2.4 Discussion

The main objective of this paper was twofold: (1) to present a non-parametric blind deconvolution method to obtain the latent neuronal response from the fMRI signal and, (2) to compare our approach to the best performing existing parametric model [32]. We hypothesized that if the results from non-parametric deconvolution closely resembled that obtained from parametric deconvolution, then the problem of over fitting during estimation in highly parameterized

deconvolution models of fMRI can be ignored. On the other hand, lack of agreement between parametric and non-parametric models would require further investigation into the problem of over-fitting in highly parameterized models. In order to test this hypothesis, we non-parametrically deconvolved both simulated and experimental fMRI signals using the concept of the cepstrum and homomorphic filtering, to obtain the latent neuronal response. It is noteworthy that this method made absolutely no assumptions, except using the fact that most of the energy in the HRF is concentrated in low frequencies while for the latent neural variables, their energies are concentrated in relatively higher frequencies. We compared the performance of the non-parametric homomorphic deconvolution method with the best parametric deconvolution method based on the CKF and hemodynamic model. Both simulations and experimental results demonstrate support for our hypothesis since the estimated latent neural response from both parametric and non-parametric methods were highly correlated. Further, simulations showed that both methods were effective in recovering the simulated ground truth. Therefore, we conclude that skepticism about the efficacy of highly parameterized blind deconvolution models of fMRI for recovering latent neuronal variables due to the problem of over-fitting is probably not justified. Future studies must perform a similar comparison between parametric and non-parametric blind deconvolution methods for fMRI using simultaneously acquired invasive electrophysiological measurements as ground truths for latent neural signals in order to verify our findings.

## Chapter 3 Effective Connectivity Model

Author contributions: Developed the model: Gopikrishna Deshpande. Implementing the model: Karthik Sreenivasan, guided by Gopikrishna Deshpande. Written by: Karthik Sreenivasan, Gopikrishna Deshpande

### 3.1 Introduction

In recent years, studies investigating the causal influence of one brain regions on another (effective connectivity (EC)) from fMRI data are increasingly being recognized as sources of vital information regarding functioning of different brain networks in both healthy and patient populations. As discussed earlier in chapter-1, various methods have been proposed for effective connectivity analysis. Some of the more frequently used methods being dynamic causal modeling (DCM) [18], structural equation modeling (SEM) [22] and Granger causality (GC) analysis [15, 17, 23, 24, 25]. However, the GC methods have certain advantages when compared to the other methods. GC being a completely data-driven method does not rely on priori information about the connectivity network model like the DCM. Secondly unlike the SEM models, increase in the number of ROIs does not affect the complexity or performance of GC analysis. In addition to this since the GC model is a stochastic model it allows for the complexities in the connectivity networks which are sometimes not accounted for by deterministic models like the DCM. These distinct advantages contributed to the increase in the prominence of the GC analysis.

GC is based on the principle that directional causal influence from time series  $A$  to time series  $B$  can be inferred if past values of time series  $A$  help predict the present and future values of the time series  $B$  [76]. Many previous studies have used multivariate autoregressive models (MVAR) to characterize the predictive relationship between time series [15, 17, 19, 23, 24, 25, 40, 41, 42, 43] [44, 45, 46, 47]. However using raw data in GC analysis could lead to confounds in the obtained causal connectivity metrics [27, 28] which can be attributed to the spatial variability of the hemodynamic response. Ensuing this, blind deconvolution has been proposed as a pre-processing step in GC analysis [28, 29, 30, 31] to remove the non-neuronal variability of the hemodynamic response [26]. Therefore, in this connectivity model, we use the hidden neuronal variables obtained after blind hemodynamic deconvolution [32] in GC analysis. We have shown two different connectivity models, a static MVAR model used to obtain static EC over the entire time series from two ROIs, and a dynamic MVAR model where the model coefficients vary as a function of time, so as to calculate EC dynamically, inferring that the causal connectivity between two ROIs is dynamically varying over time.

## 3.2 Connectivity model

### 3.2.1 Blind deconvolution model

Let  $p$  fMRI time series be represented as  $Y(t) = [y_1(t) \ y_2(t) \ \dots \ y_p(t)]$ . A dynamic state-space model can be described as follows.

$$\tilde{n}_\Gamma^p = \begin{bmatrix} n_\Gamma^p \\ r_\Gamma^p \\ \theta_\Gamma^p \end{bmatrix} = \begin{bmatrix} \mathbf{f}(n_{\Gamma-1}^p, r_{\Gamma-1}^p, \theta_{\Gamma-1}^p) \\ r_{\Gamma-1}^p \\ \theta_{\Gamma-1}^p \end{bmatrix} + \begin{bmatrix} L_{\Gamma-1}^p \\ K_{\Gamma-1}^p \\ J_{\Gamma-1}^p \end{bmatrix} \quad (1)$$

Where  $n$  is the neuronal state variable,  $r$  is the exogenous input and  $\theta$  is the parameter variables.  $f$  is the function which links the current neuronal state to the previous neuronal states, exogenous inputs and parameters. The subscript  $\Gamma$  indicates continuous time and the superscript  $p$  indicates the number of time series in the model.  $L$ ,  $K$  and  $J$  are the zero mean Gaussian state noise vectors. The observation equation, which links the state to observation variables, is as follows.

$$y_p(t) = \mathbf{m}(\tilde{\mathbf{n}}_t^p) + v_{t-1} \quad (2)$$

Here the state variables and the measurement variables are linked by the function  $\mathbf{m}$ . The variables  $t$  and  $v$  represent the discrete time and measurement noise, respectively. The exogenous inputs  $r$  (i.e. experimental boxcar function) and fMRI time series  $y_p(t)$  are the inputs to the model. In case of resting state studies there is no experimental boxcar function (exogenous input). Therefore the input to the model is only the fMRI time series  $y_p(t)$  and Eq. 1 can be rewritten as shown in Eq. 3.

$$\tilde{\mathbf{n}}_{\Gamma}^p = \begin{bmatrix} n_{\Gamma}^p \\ \theta_{\Gamma}^p \end{bmatrix} = \begin{bmatrix} f(n_{\Gamma-1}^p, \theta_{\Gamma-1}^p) \\ \theta_{\Gamma-1}^p \end{bmatrix} + \begin{bmatrix} L_{\Gamma-1}^p \\ J_{\Gamma-1}^p \end{bmatrix} \quad (3)$$

As shown before, the Cubature Kalman Filter (CKF) performs very efficient joint estimation of underlying neuronal state variables and parameters [32]. Also, by using a smaller time step (10 times smaller than the TR) while discretizing the continuous time model, the neuronal variables can be successfully estimated at an effective temporal resolution. Using such neuronal variables with high temporal resolution in an MVAR model enables effective connectivity analysis.

### 3.2.2 Static MVAR model

The neuronal state variables  $n_p(t)$  can be input into the MVAR as follows

$$\begin{bmatrix} n_1(t) \\ n_2(t) \\ \vdots \\ n_p(t) \end{bmatrix} = \begin{bmatrix} 0 & a_{12}^{(0)} & \dots & a_{1p}^{(0)} \\ a_{21}^{(0)} & 0 & & a_{2p}^{(0)} \\ \vdots & \vdots & 0 & \vdots \\ a_{p1}^{(0)} & a_{p2}^{(0)} & \dots & 0 \end{bmatrix} \times \begin{bmatrix} n_1(t) \\ n_2(t) \\ \vdots \\ n_p(t) \end{bmatrix} + \sum_{s=1}^{\omega} \begin{bmatrix} a_{11}^{(s)} & a_{12}^{(s)} & \dots & a_{1p}^{(s)} \\ a_{21}^{(s)} & a_{22}^{(s)} & & a_{2p}^{(s)} \\ \vdots & \vdots & \ddots & \vdots \\ a_{p1}^{(s)} & a_{p2}^{(s)} & \dots & a_{pp}^{(s)} \end{bmatrix} \times \begin{bmatrix} n_1(t-s) \\ n_2(t-s) \\ \vdots \\ n_p(t-s) \end{bmatrix} + \begin{bmatrix} \delta_1(t) \\ \delta_2(t) \\ \vdots \\ \delta_p(t) \end{bmatrix} \quad (4)$$

Where  $\omega$  is the order of the model determined by the Akaike/Bayesian information criterion [77, 78],  $a$  are the model coefficients and  $\delta$  is the model error. Note that  $a(0)$  represent the instantaneous influences between time series while  $a(s)$ ,  $s=1 \dots \omega$  represent the causal influences between time series. By modeling both instantaneous and causal terms in a single model, effect of instantaneous correlation on causality can be minimized [79]. The coefficients of the model  $a_{ij}(s)$ ,  $i, j = 1 \dots p$  are determined in the least square sense. The static causal influence (correlation purged GC (CPGC)) between the  $p$  time series can be calculated using the model coefficients as shown in Eq. 5

$$CPGC_{ij} = \sum_{s=1}^{\omega} [a_{ij}(s)]^2 \quad (5)$$

### 3.2.3 Dynamic MVAR model

The MVAR model can be made dynamic by allowing the model coefficients to vary as a function of time as given below (Eq. 6).

$$\begin{bmatrix} n_1(t) \\ n_2(t) \\ \vdots \\ n_p(t) \end{bmatrix} = \begin{bmatrix} 0 & a_{12}^{(0,t)} & \dots & a_{1p}^{(0,t)} \\ a_{21}^{(0,t)} & 0 & & a_{2p}^{(0,t)} \\ \vdots & \vdots & 0 & \vdots \\ a_{p1}^{(0,t)} & a_{p2}^{(0,t)} & \dots & 0 \end{bmatrix} \times \begin{bmatrix} n_1(t) \\ n_2(t) \\ \vdots \\ n_p(t) \end{bmatrix} + \sum_{s=1}^{\omega} \begin{bmatrix} a_{11}^{(s,t)} & a_{12}^{(s,t)} & \dots & a_{1p}^{(s,t)} \\ a_{21}^{(s,t)} & a_{22}^{(s,t)} & & a_{2p}^{(s,t)} \\ \vdots & \vdots & \ddots & \vdots \\ a_{p1}^{(s,t)} & a_{p2}^{(s,t)} & \dots & a_{pp}^{(s,t)} \end{bmatrix} \times \begin{bmatrix} n_1(t-s) \\ n_2(t-s) \\ \vdots \\ n_p(t-s) \end{bmatrix} + \begin{bmatrix} \delta_1(t) \\ \delta_2(t) \\ \vdots \\ \delta_p(t) \end{bmatrix} \quad (6)$$

The model coefficients  $a_{ij}(s,t)$  were taken as the state vector of a Kalman filter and adaptively estimated using the algorithm proposed by Arnold et al [80]. Dynamic Granger causality (DGC) was then obtained as follows

$$DGC_{ij}(t) = \sum_{s=1}^{\omega} [a_{ij}(s,t)] \quad (7)$$

### 3.3 Connectivity Analysis

Initially the mean fMRI time series are extracted from the regions of interest (ROIs) for all participants. These average time series are then temporally normalized and input to the deconvolution model. In this step the fMRI time series are deconvolved using the CKF and the latent neuronal variables are obtained. These latent neuronal variables are then input into the

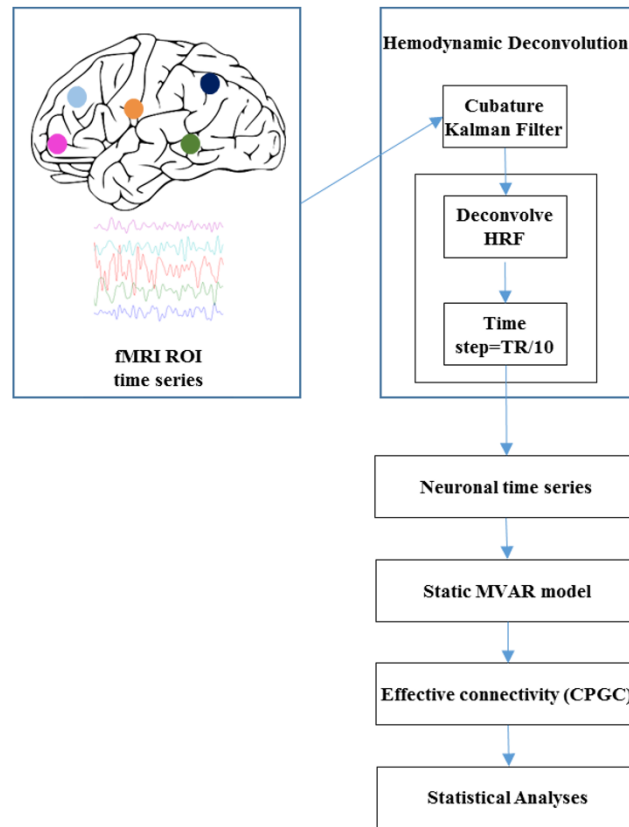


**Fig 3.1** CPGC connectivity analysis

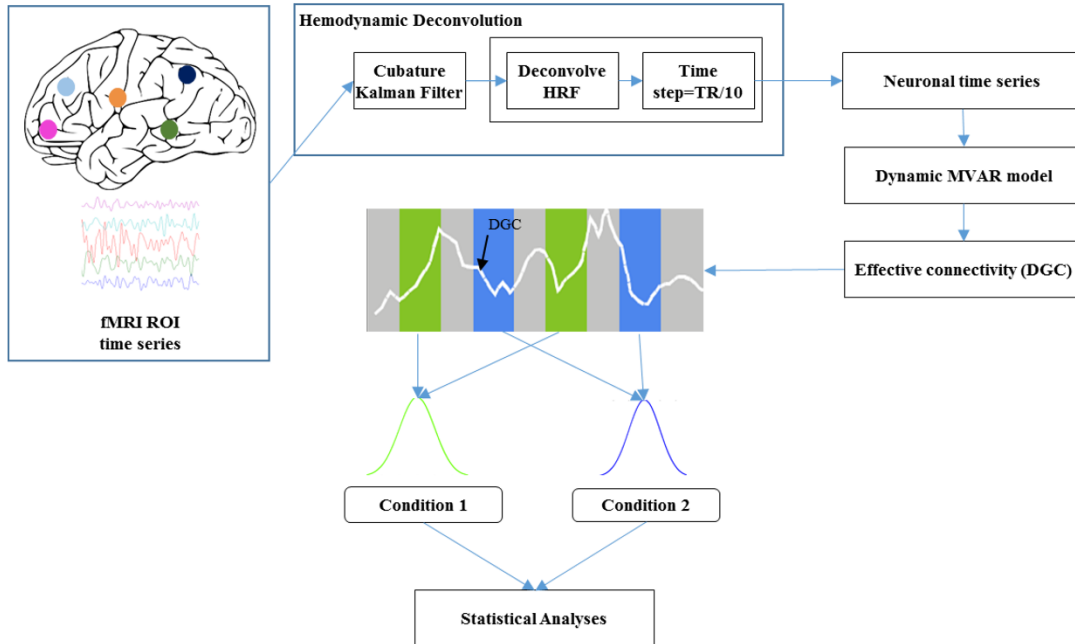


**Fig 3.2** DGC connectivity analysis. The green and blue bars represent two different conditions (condition 1 and condition 2).

MVAR model to obtain the granger causal metrics. In case of CPGC analysis (static MVAR model) the causal connectivity values obtained can then be statistically analyzed for forming inferences. Figure 3.1 shows the schematic for CPGC analysis. For DGC since we obtain the connectivity values over time they can be populated into different samples corresponding to particular conditions and then be statistically compared to infer the causal connectivity between the different regions with respect to the different conditions. The schematic for DGC analysis is shown in figure 3.2. The two different conditions (condition 1 and condition 2) are represented by green and blue bars respectively.

## **Chapter 4 Applications of the granger causality based effective connectivity model**

### **4.1 Identification of neural connectivity signatures of autism using machine learning**

This study was done in collaboration with Lauren Libero, Hrishikesh Deshpande and Dr. Rajesh Kana. All the above mentioned collaborators are from the University of Alabama - Birmingham, Birmingham, AL. This work has been published in the journal *Frontiers in Human Neuroscience*. My main contributions to this paper are effective connectivity analysis of the data and help writing the paper, under the guidance of Dr. Gopikrishna Deshpande.

#### **4.1.1 Introduction**

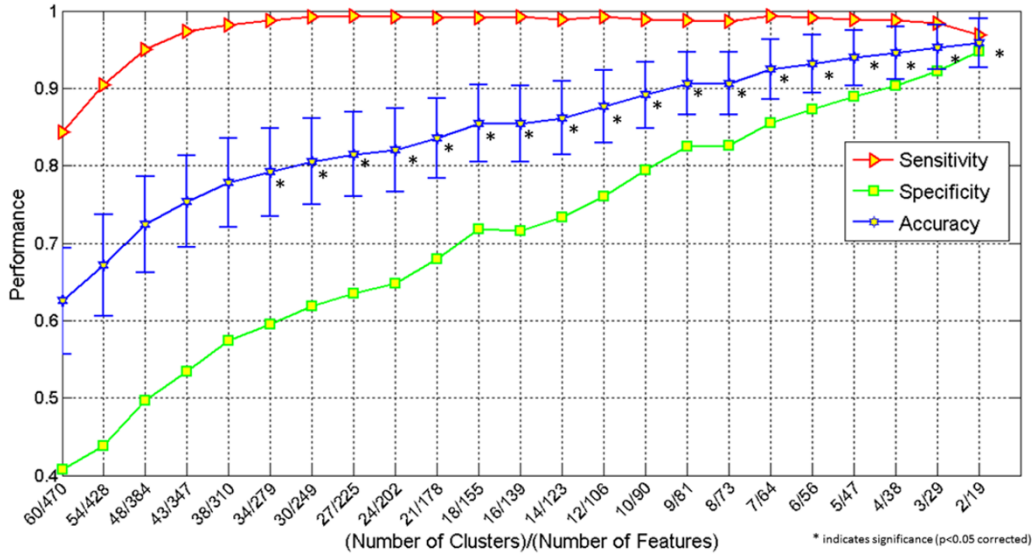
Interregional connectivity abnormalities have been suggested as a neural signature of the pathobiology of autism [81, 82]. There have been many reports of functional and anatomical connectivity being altered in complex cognitive and social tasks in autism. Although disrupted instantaneous correlation between cortical regions observed from functional MRI of the autistic brain is considered to be an explanatory model for autism, the causal influence of a brain area on another (effective connectivity (EC)) is a vital link which is missing in these studies. The current study focuses on addressing this in an fMRI study of Theory-of-Mind (ToM) in high-functioning adults with autism. Importantly, statistical separation of neural signatures (e.g. t-test) demonstrated in previous studies do not guarantee generalizability or predictive power of those signatures for diagnosis. Therefore, we adopt machine learning approaches for identification of neural signatures which can accurately classify individuals with autism from individuals with typical development.

### 4.1.2 Materials and Methods

Participants viewed a series of comic strip vignettes in the MRI scanner and were asked to choose the most logical end to the story from three alternatives, separately for trials involving physical and intentional causality. For physical causality condition, participants relied on laws of physics to arrive at their judgment and in the case of intentional causality they relied on social rules or ToM. 15 typically developing (TD) control participants and 15 high functioning adults with autism were scanned using a standard EPI sequence on a 3T Siemens Allegra scanner (TR = 1000ms, TE = 30ms, flip angle = 60 degrees). After standard pre-processing and activation analysis, mean time series were extracted from 18 activated regions of interest (ROIs) and the correlation purged granger causality (CPGC) metrics for all participants were obtained by applying the method discussed in chapter-3. First, the averaged time series were normalized and input to the deconvolution model to obtain the underlying neuronal variables using Cubature Kalman filter (CKF) based blind hemodynamic deconvolution [32]. The resultant neural response was input into a static multivariate autoregressive model (MVAR) [47, 79] to obtain the causality matrices for each of the 30 participants. These causal connectivity weights, along with assessment scores (Autism Spectrum Quotient (AQ) and Reading the Mind in the Eyes (RME)), functional connectivity values, and fractional anisotropy obtained from DTI data for each participant (all the other metrics except for effective connectivity were obtained earlier in another study [83]) were then input into a recursive cluster elimination based support vector machine (RCE-SVM) classifier [84] to determine the accuracy with which the classifier can predict a novel subject's group membership (autism or control).

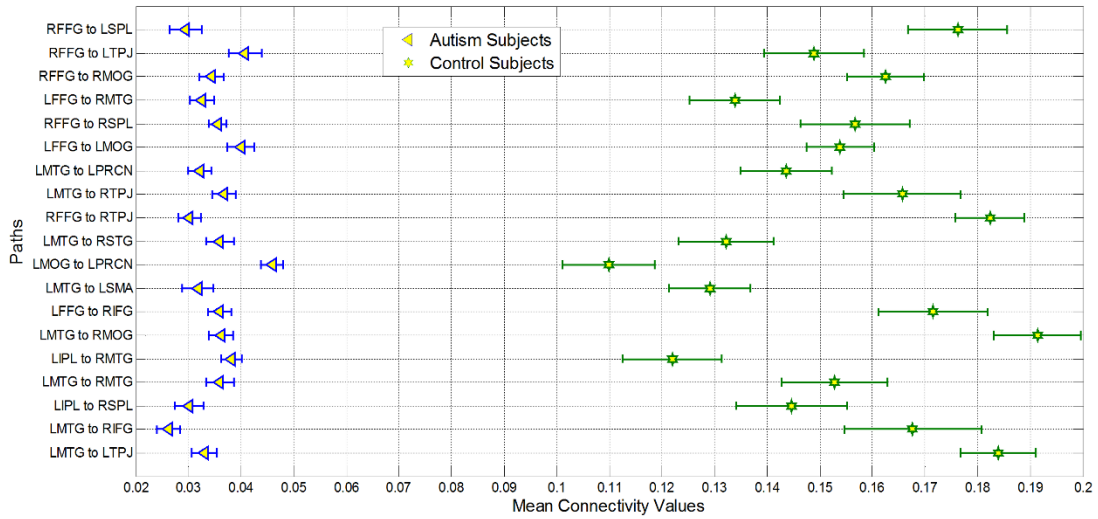
### 4.1.3 Results

Figure 4.1 demonstrates the increase of classification accuracy as the number of features is decreased. Utilizing 2 feature clusters comprised of 19 metrics, the classification accuracy reached a maximum accuracy of 95.9% (specificity 94.8% and sensitivity 96.9%) and all of these 19 metrics were effective connectivity paths.



**Figure 4.1** Graph showing classification accuracy, sensitivity and specificity obtained by simultaneously using the following features: behavioral scores, functional connectivity, effective connectivity and fractional anisotropy obtained from DTI. The X-axis shows number of clusters/number of features and the Y-axis, the performance (classification accuracy, sensitivity and specificity).

The causal connectivity value of these 19 paths which lead to maximum accuracy showed clear separation between participants with autism (blue) and control participants (green) (figure 4.2), with these paths showing significantly ( $p < 0.05$ ) weaker connectivity in participants with autism compared to TD controls. The 19 effective connectivity paths which were most important in classification are shown in figure 4.3 (Plotted using brainnet viewer [85]).



**Figure 4.2** Mean of nineteen paths which was most important for giving maximum classification accuracy for autism and control groups. All paths had significantly decreased connectivity ( $p < 0.05$  corrected using Bonferroni method for 18 paths; for one of the paths  $p < 0.05$  uncorrected) in the Autism group as compared to controls. The bars represent standard errors.

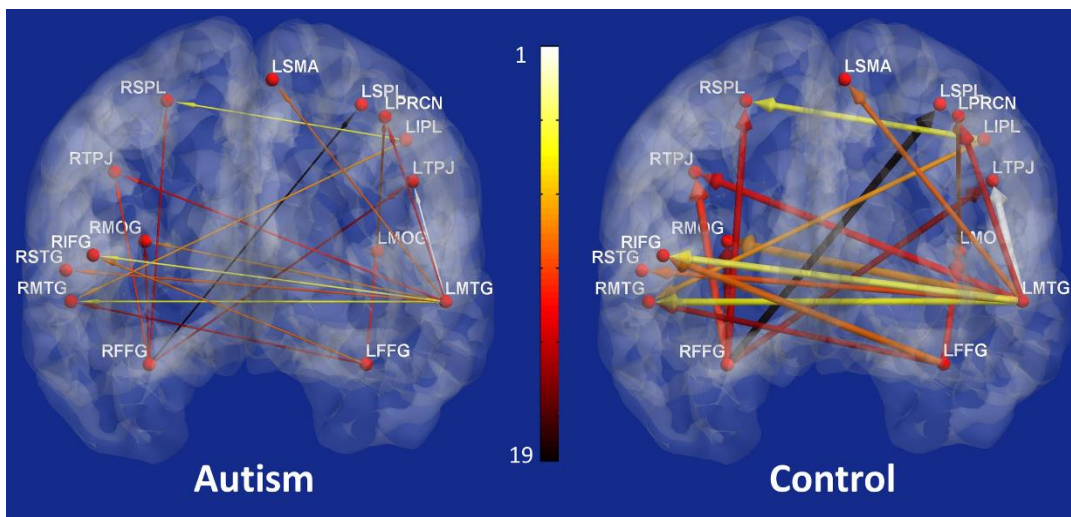


**Figure 4.3** The nineteen paths whose effective connectivity values were top-ranked features for classification of the two groups (Autism and Controls) with the maximum accuracy (Left panel: participants with autism; and right panel: control participants). The width of the arrows represents the path strength and the color of the path indicates its rank obtained during classification with 1 being the most significant and 19 being the least significant.

A Spearman’s non-parametric correlation was also performed between the 19 features that were ranked highest in classification and assessment scores (AQ and RME). Table 4.1 shows the correlation coefficients and p-values for the specific paths. We can see that there was a significant

negative correlation between EC paths and the AQ scores as well as a significant positive correlation between EC paths and the RME scores.

Paths correlated with Autism Quotient (AQ) scores				Paths correlated with Reading Mind in Eye (RME) scores					
<u>Source Region</u>	→	<u>Sink Region</u>	<u>p-value</u>	<u>Correlation Coefficient</u>	<u>Source Region</u>	→	<u>Sink Region</u>	<u>p-value</u>	<u>Correlation Coefficient</u>
LMTG	→	LTPJ	0.0003	-0.6137	LMTG	→	LTPJ	0.0311	0.3941
LMTG	→	RIFG	0.0007	-0.5837	LMTG	→	RIFG	0.0183	0.4279
LMTG	→	RMTG	0.0001	-0.6466	LMTG	→	RMTG	0.0455	0.3679
LMTG	→	RMOG	0.0006	-0.5901	LMTG	→	RMOG	0.0325	0.3912
LFFG	→	RIFG	0.0061	-0.4889	LFFG	→	RIFG	0.0428	0.3723
LMTG	→	LSMA	0.0006	-0.5930	LMTG	→	LSMA	0.0421	0.3734
RFFG	→	RTPJ	0.0028	-0.5274	RFFG	→	RTPJ	0.0373	0.3819
LFFG	→	RMTG	0.0119	-0.4531	LFFG	→	RMTG	0.0151	0.4395
RFFG	→	RMOG	0.0098	-0.4642	RFFG	→	RMOG	0.0035	0.5169
RFFG	→	LSPL	0.0187	-0.4266	RFFG	→	LSPL	0.0417	0.3741
LMTG	→	RSTG	0.0391	-0.3785	LIPL	→	RSPL	0.0082	0.4735
LMTG	→	RTPJ	0.0319	-0.3926	LFFG	→	LMOG	0.0213	0.4186
					RFFG	→	RSPL	0.0425	0.3727

**Table 4.1** Paths correlated with Autism Quotient (AQ) scores and Reading Mind in Eye (RME) scores. The paths in red were correlated with both AQ and RME.

#### 4.1.4 Discussion

The main results of this study are summarized as follows: (1) The effective connectivity metrics were able to successfully classify participants by diagnosis with 95.9% accuracy. These path weights were the most significant features among all the different metrics used in classification; (2) Effective connectivity was significantly reduced in autistic participants compared to typical control participants; and (3) The paths that were among the top ranked features in the classification analysis were found to be significantly negatively correlated with the Autism Quotient (AQ) and positively correlated with Reading the Mind in the Eyes (RME) test scores suggesting that as autism symptom severity increased, the effective connectivity decreased; and as the theory-of-

mind ability increased, effective connectivity also increased. These findings collectively point towards the fact that alterations in causal connectivity in the brain in autism could serve as a potential non-invasive neuroimaging signature for autism.

## **4.2 A Framework for Causal Connectivity Analysis of fMRI in Patient Populations: An application to Major Depression and Early Life stress**

This study was done in collaboration with Dr. Merida Grant, David White, Jennifer Hadley, Nathan Hutcheson and Dr. Richard Shelton. All the above mentioned collaborators are from the University of Alabama - Birmingham, Birmingham, AL. This work has been published in Human Brain Mapping. My main contributions to this work is effective connectivity analysis of the data and help writing the paper, under the guidance of Dr. Gopikrishna Deshpande.

### **4.2.1 Introduction**

Differential pathophysiology within major depression (MDD) based on early life stress history is associated with two distinct phenotypes; (I) a hyper-responsive subtype characterized by exaggerated amygdala reactivity and decreased anterior cingulate (BA 32/24) volume among trauma-exposed MDD and (II) a hypo-responsive subtype associated with attenuated limbic reactivity and unaffected cingulate volume among never trauma-exposed MDD [86, 87]. Translational models of stress [88] as well as imaging findings in non-clinical human studies [89] have demonstrated key roles for medial and lateral prefrontal cortex (PFC) (e.g., anterior cingulate and dorsal lateral PFC) in modulation of limbic response to stress. The current study investigated whether differential amygdala reactivity within MDD based on early life stress history was associated with failure of inhibition from medial or lateral PFC.

### 4.2.2 Materials and Methods

Twenty un-medicated patients with MDD and 19 healthy controls performed a gender identification variant of the Eriksen flanker task of selective attention [90]. The task was designed to identify the influence of valence on the efficiency of selective attention by emotion (positive, negative, and neutral) and level of task difficulty (non-conflict, congruent and incongruent). The participants were asked to respond as quickly and accurately with a button press to identify gender centralized target faces. fMRI data were acquired on a 3T Philips Intera Achieva scanner (TR/TE/flip angle/FOV/slice thickness = 3000ms/28ms/90°/24cm/4mm). The mean time series were extracted from 11 different activated regions of interest (ROIs) for all participants and dynamic granger causality (DGC) measures were obtained by using the model discussed in chapter-3. Initially the underlying neuronal response for these times series were obtained by normalizing them and deconvolving the hemodynamic response using a CKF [32]. This was then input into a dynamic multivariate autoregressive model (dmVAR) [31, 45, 91] to obtain the connectivity matrices which were then populated into different samples (negative and neutral valence of non-conflict difficulty), separately for patients and controls. T-tests were performed between the samples and paths significantly greater during negative valence condition as compared to neutral valence were identified. Among these paths, those that were significantly different between controls and MDD patients were obtained ( $p < 0.05$ ). A schematic of the analysis procedure

is illustrated in figure 4.4. These set of paths were then examined to see if they were significantly correlated with childhood trauma scores.

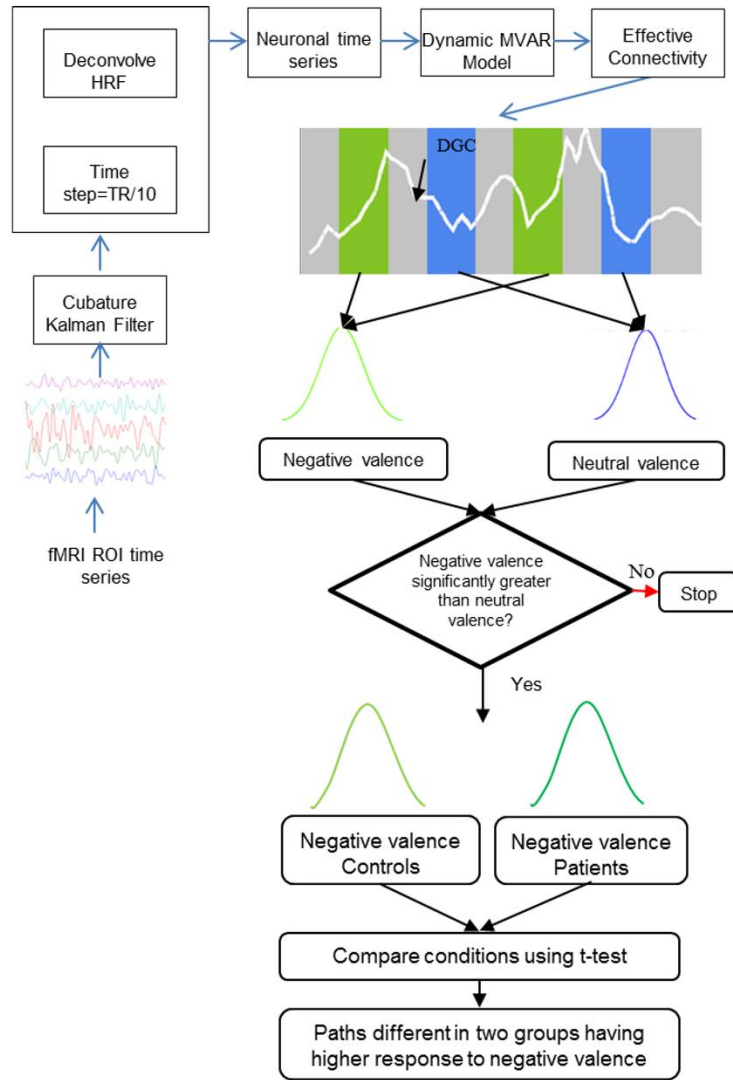


**Figure 4.4** Effective connectivity schematic

### 4.2.3 Results

Figures 4.5 and 4.6 show the paths which were significantly greater in MDD and controls, respectively, and at the same time also greater during negative valence condition. Paths originated

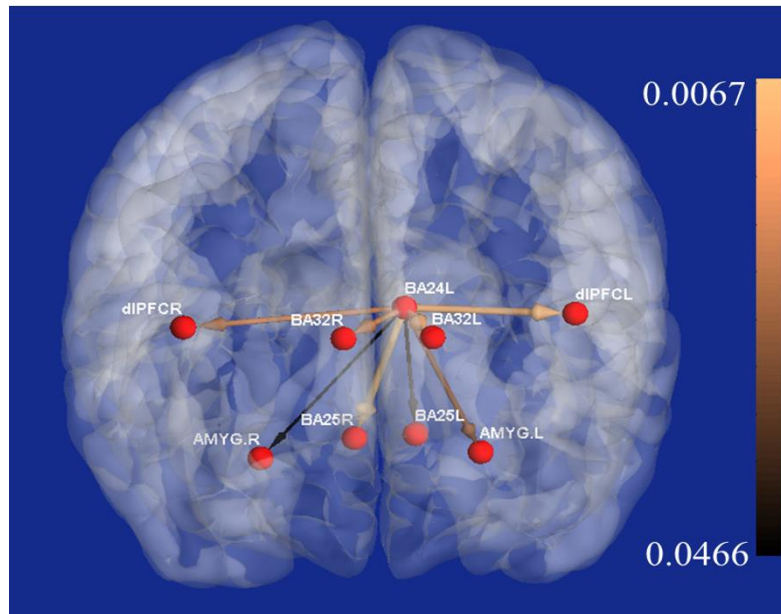


**Figure 4.5** Paths which are significantly greater in MDD patients.

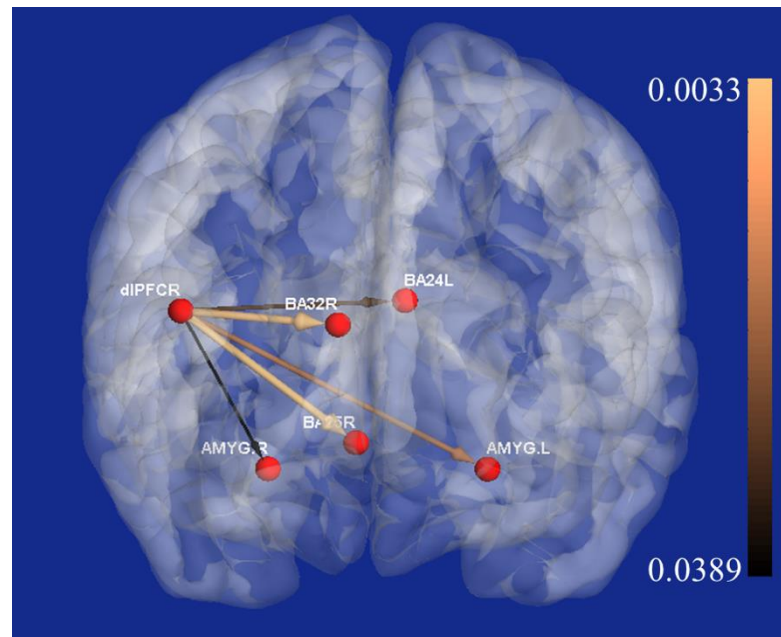


**Figure 4.6** Paths which are significantly greater in Healthy controls.

from left Brodmann area 24 (BA24L) were significantly greater in MDD, whereas outputs from right dorsolateral PFC (dlPFC R) were greater in controls. Figure 4.7 shows the significant correlation ( $p < 0.05$ ) for physical neglect and left BA 32-right dlPFC connectivity. Similarly figure

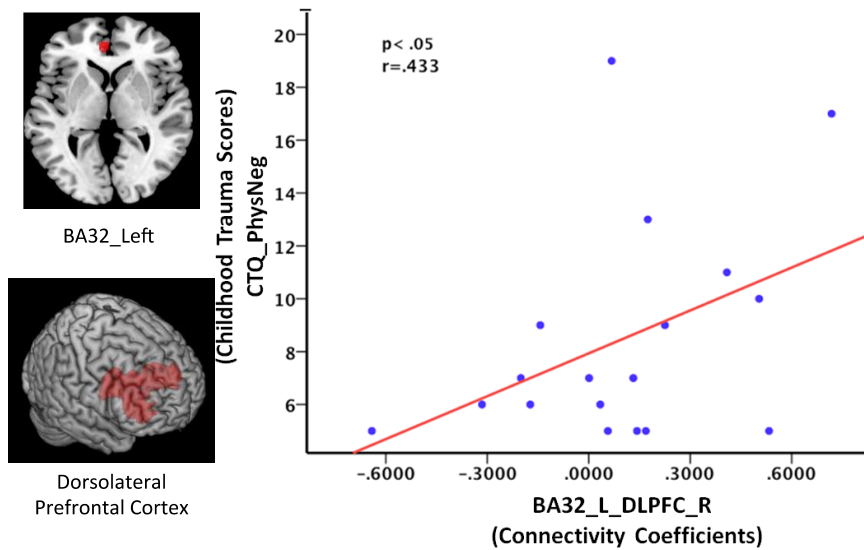


**Figure 4.7** Relationship between early life trauma and mPFC-DLPFC connectivity. Correlations within MDD between ELT history and mPFC-dlPFC indicating an inverse relationship between medial and lateral PFC among non-ELT exposed depressed but a positive correlation for ELT-exposed depressed.

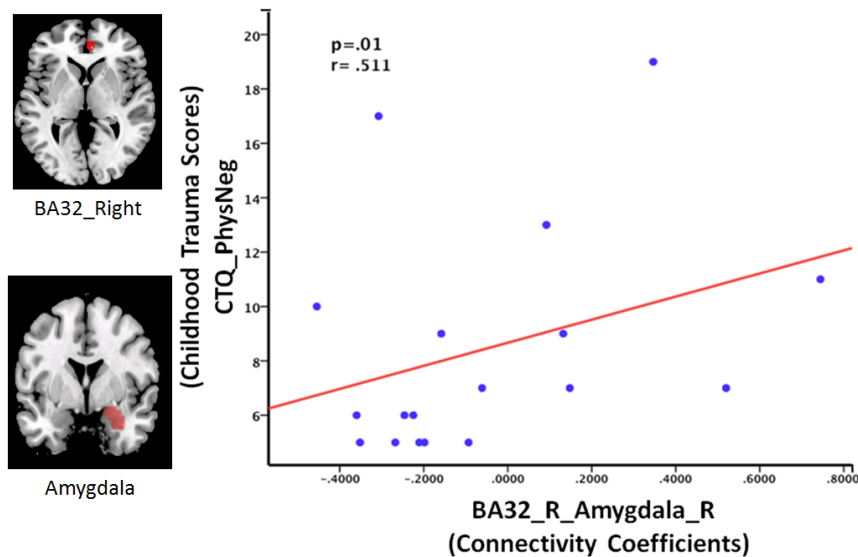


**Figure 4.8** Relationship between early life trauma and mPFC-amygdala connectivity. Correlations within MDD between ELT history and mPFC-amygdala indicating an inverse relationship between medial PFC and amygdala among non-ELT exposed depressed but a positive correlation for ELT-exposed depressed.

4.8 shows significant correlation ( $p < 0.01$ ) between the physical neglect with right BA32-right amygdala connectivity.

#### **4.2.4 Discussion**

The current investigation revealed between group differences in directional connectivity in response to aversive stimuli among MDD and HC. Specifically, inputs to amygdala from lateral PFC was higher in HC and from medial PFC was higher in MDD. Positive correlation of the path from medial PFC to amygdala with early life trauma in MDD supports the view that differential amygdala reactivity within MDD based on early life stress history is associated with failure of top-down inhibition.

### **4.3 Effective connectivity reveals learning-related changes in the emotional response to a threat**

This study was done in collaboration with Muriah Wheelock, Kimberly Wood, Dr. Lawrence Ver Hoef, and Dr. David Knight. All the above mentioned collaborators are from the University of Alabama - Birmingham, Birmingham, AL. This work will be submitted to NeuroImage. My main contributions to this study is effective connectivity analysis of the data and help writing the paper, under the guidance of Dr. Gopikrishna Deshpande.

#### **4.3.1 Introduction**

Recognizing cues that predict aversive events allows one to react more effectively under threatening conditions. Prior work has demonstrated that dorsolateral prefrontal cortex (dlPFC), dorsomedial PFC (dmPFC), posterior cingulate cortex (PCC), anterior cingulate cortex (ACC),

anterior insula, amygdala, and inferior parietal lobule (IPL) showed a diminished response to predictable aversive events (100db white noise) [89]. The present study examined the causal relationships within this brain network in response to predictable and unpredictable unconditioned stimulus (UCS) presentations.

#### **4.3.2 Materials and Methods**

Twenty-four healthy right-handed volunteers participated in this fear conditioning study [89]. Participants were exposed to a fear conditioning procedure during which two distinct tones (700 and 1300 Hz) served as the conditioned stimuli (CSs). One tone (CS+) coterminated with a white noise (100dB) UCS and the second tone (CS-) was presented without the UCS. During the test trials, the CS+ coterminated with the UCS (CS+UCS), CS- coterminated with the UCS (CS-UCS), and the UCS was presented alone (UCS alone) to assess conditioned diminution of the unconditioned response (UCR). Functional magnetic resonance imaging (fMRI) data were acquired on a 3 Tesla Siemens Allegra scanner (TR/TE/flip angle/FOV/slice thickness = 2000ms/30ms/70°/24cm/4mm). Image processing was executed using AFNI [92]. The mean time series from fifteen activated regions of interest (ROIs) was extracted for all participants and DGC was obtained as discussed in chapter-3. The time series were temporally normalized and then the hidden neuronal variables were obtained by deconvolving the fMRI time series using a CKF [32]. This neuronal response was then input into a dMVAR [31, 45, 91] to obtain dynamic connectivity between every pair of ROIs. In order to find task-specific connectivity, causality values were populated into three different samples based on the UCS alone, CS+UCS, and CS-UCS (test trials) conditions. An ANOVA was performed on these samples to find the paths which were significantly different between trial type ( $p < .05$ ). On these paths one sample and two sample t-tests were performed to find the paths significant within trial type ( $p < 0.05$ ) and significantly different

between the CS+UCS and UCS alone trial types ( $p < .01$ ). Schematic of the analysis is shown in figure 4.9.

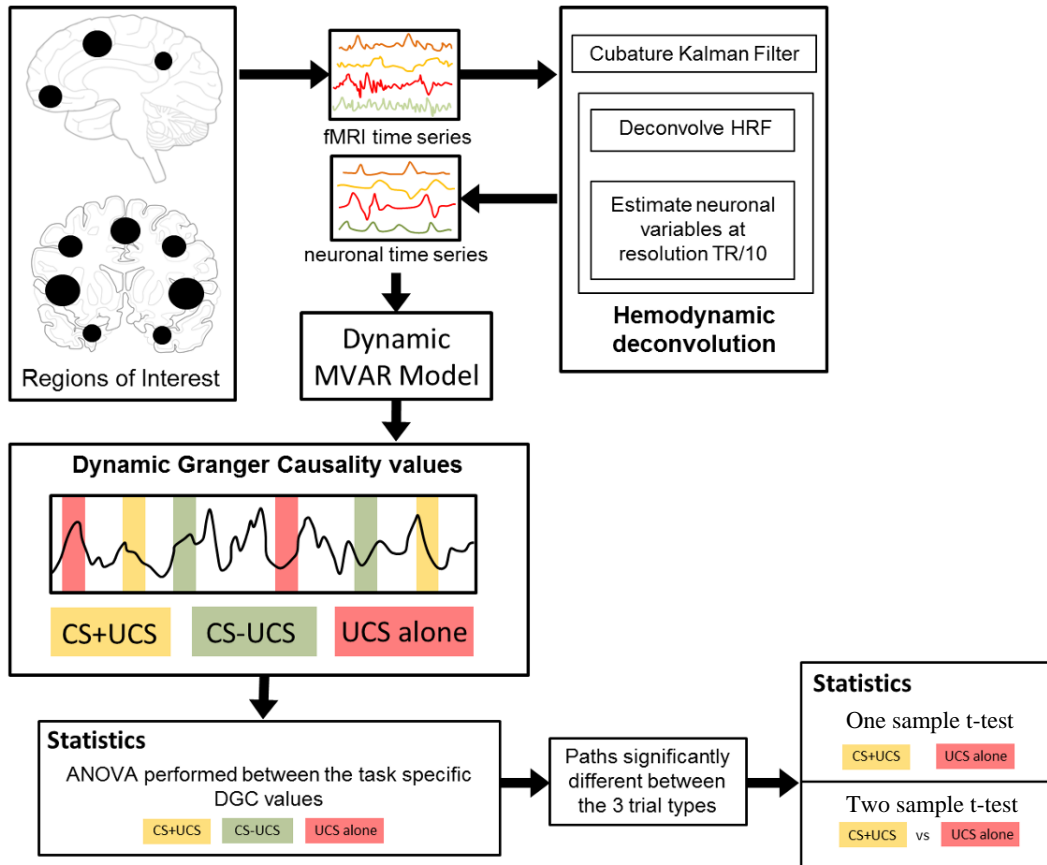


**Figure 4.9** Effective connectivity analysis schematic

### 4.3.3 Results

Analyses of CS+UCS and UCS alone revealed two main source ROI; the dlPFC and ACC. For simplicity, all figures and results present connections emanating from these sources only. Presentations of the CS+UCS showed greater connectivity than UCS alone from dlPFC to insula,

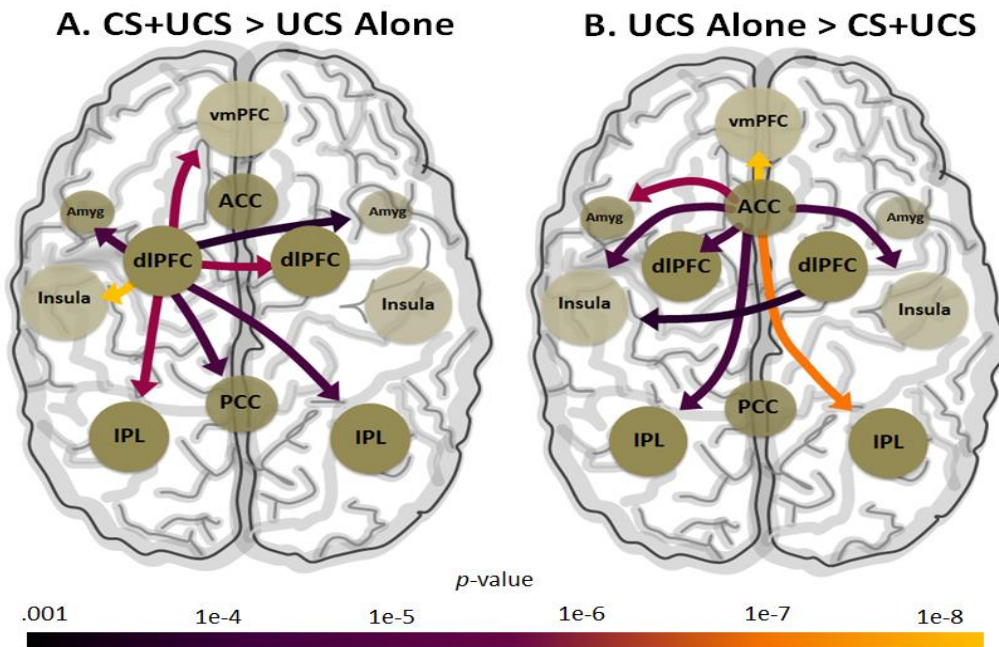


**Figure 4.10** A) Greater connectivity during a predictable UCS than during an unpredictable UCS. B) Greater connectivity during an unpredictable UCS than during a predictable UCS. Diagrams are in neurologic view (right hemisphere is on right)

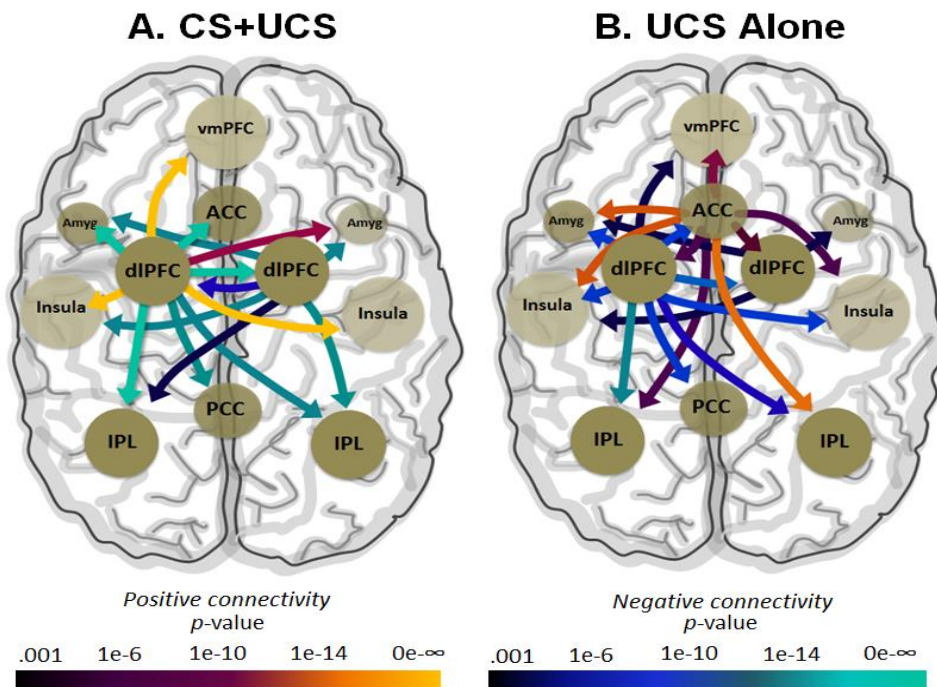


**Figure 4.11** Significant connectivity within trial type ( $p < .01$ ). Warm colors indicate positive relationship and cool colors indicate negative relationship. A) Significant connectivity during a predictable UCS (CS+UCS). B) Significant connectivity during an unpredictable UCS (UCS alone). Diagrams are in neurologic view (right hemisphere is on right)

PCC, ventromedial PFC (vmPFC), amygdala, and IPL (figure 4.10A). UCS alone compared to the

CS+UCS showed greater connectivity from ACC to vmPFC, dlPFC, amygdala, insula, and IPL (figure 4.10B). Examination of within trial type effects showed that presentations of CS+UCS mainly elicited negative connections from dlPFC (figure 4.11A). Analysis of UCS alone revealed similar negative correlations emanating from the dlPFC (figure 4.11B). However, during UCS alone condition, the ACC showed a lot of positive connections not present during CS+UCS (figure 4.11B).

#### **4.3.4 Discussion**

The ACC showed significantly greater top-down connectivity to vmPFC and amygdala during unpredictable presentations of the UCS alone than during predictable CS+UCS presentations (figure 4.10B). Further investigation revealed that when the UCS was unpredictable, activation within the ACC resulted in increased activation of brain regions including the amygdala and vmPFC (figure 4.11B). These results are consistent with literature suggesting the ACC signals an aversive event and coordinates other regions to take action during an unpredicted adverse event [93]. In contrast, the left dlPFC was significantly more involved in top-down regulation of other brain regions during CS+UCS trials compared to UCS alone (figure 4.10A). When the UCS was predictable, dlPFC activation resulted in decreased activation within the amygdala and IPL (figure 4.11A), consistent with an executive down-regulation of amygdala activity during a predictable adverse event [94].

#### **4.4 Effective connectivity analysis of the memory network in schizophrenia before and after antipsychotic medication**

This study was done in collaboration with Nathan Hutcheson, Jennifer Hadley, Dr. Mark Bolding, David White, Dr. Lawrence Ver Hoef and Dr. Adrienne Lahti. All the above mentioned collaborators are from the University of Alabama - Birmingham, Birmingham, AL. This work will be submitted to Human Brain Mapping. My main contributions to this paper are effective connectivity analysis of the data and helping to write the paper, under the guidance of Dr. Gopikrishna Deshpande.

#### **4.4.1 Introduction**

Schizophrenia is characterized by positive, negative, and cognitive symptoms. The positive symptoms are present as hallucinations, delusions, and disorganization in thought and behavior which usually attract the most attention. While the negative symptoms include a lack of motivation, poverty of speech, lack of pleasure, and social withdrawal. Also, patients with schizophrenia exhibit cognitive impairments, which cover a variety of mental capacities including executive function, attention, and memory which are often present at the initial diagnosis [95]. Also, despite the large focus on positive symptoms such as hallucinations and delusions, research has shown that cognitive deficits such as attention and memory dysfunction are actually more predictive of long-term outcome [96, 97] and the neural mechanisms behind these cognitive deficits still remain unclear [98]. Previous work has shown that patients with schizophrenia (SZ) have memory disruptions, which often do not improve with antipsychotic medication. Reports have suggested that disrupted functional and anatomical connectivity could help explain these memory disturbances. Even though these findings are useful to map out neural connections altered in schizophrenia, they do not help to distinguish between the directions of these connections in the brain. In the current study we explored the causal influences between brain regions that underlie episodic memory in healthy controls and participants with schizophrenia both off medication and

after 1-week of antipsychotic medication. We investigated if participants with schizophrenia showed significant alterations within the memory network compared to healthy controls and whether these connections improved with medication.

#### **4.4.2 Materials and Methods**

Functional magnetic resonance imaging (fMRI) data was collected during an episodic memory in 21 off-medication SZ and 20 healthy controls (HC) and 16 SZ that had data both before and after 1-week of APD treatment. All imaging was performed on a 3 Tesla Siemens Allegra scanner (TR/TE/flip angle/FOV/slice thickness = 2100ms/30ms/70°/24cm/4mm). The mean time series were extracted from 11 activated regions of interest relevant during an episodic memory task, and the DGC values were obtained by using the connectivity model discussed in the previous chapter. Initially, these average time series were normalized and deconvolved using the CKF [32] to obtain the hidden neuronal variables, which were then input into the dMVAR model [31, 45, 91] to obtain time-varying connectivity metrics for each of the healthy controls and participants with schizophrenia (both before and after medication). The causal connectivity values obtained were then populated into different samples corresponding to retrieve old correct (ROC) and retrieve new correct (RNC) conditions for HC and SZ (before and after medication) groups respectively. Separate t-tests were performed between these samples in each of the following groups: controls, schizophrenia before medication and schizophrenia after medication. Only the paths which were significantly greater ( $p < 0.05$ ) in the ROC condition as compared to RNC condition were considered for further statistical comparisons. For the paths identified above, we performed 2 two-sample t-tests using the samples derived from ROC connectivity values to obtain

the difference in connectivity between the following groups: (1) HC and SZ before medication (2) SZ before medication and SZ after medication. A schematic of the analysis is shown in figure 4.12.

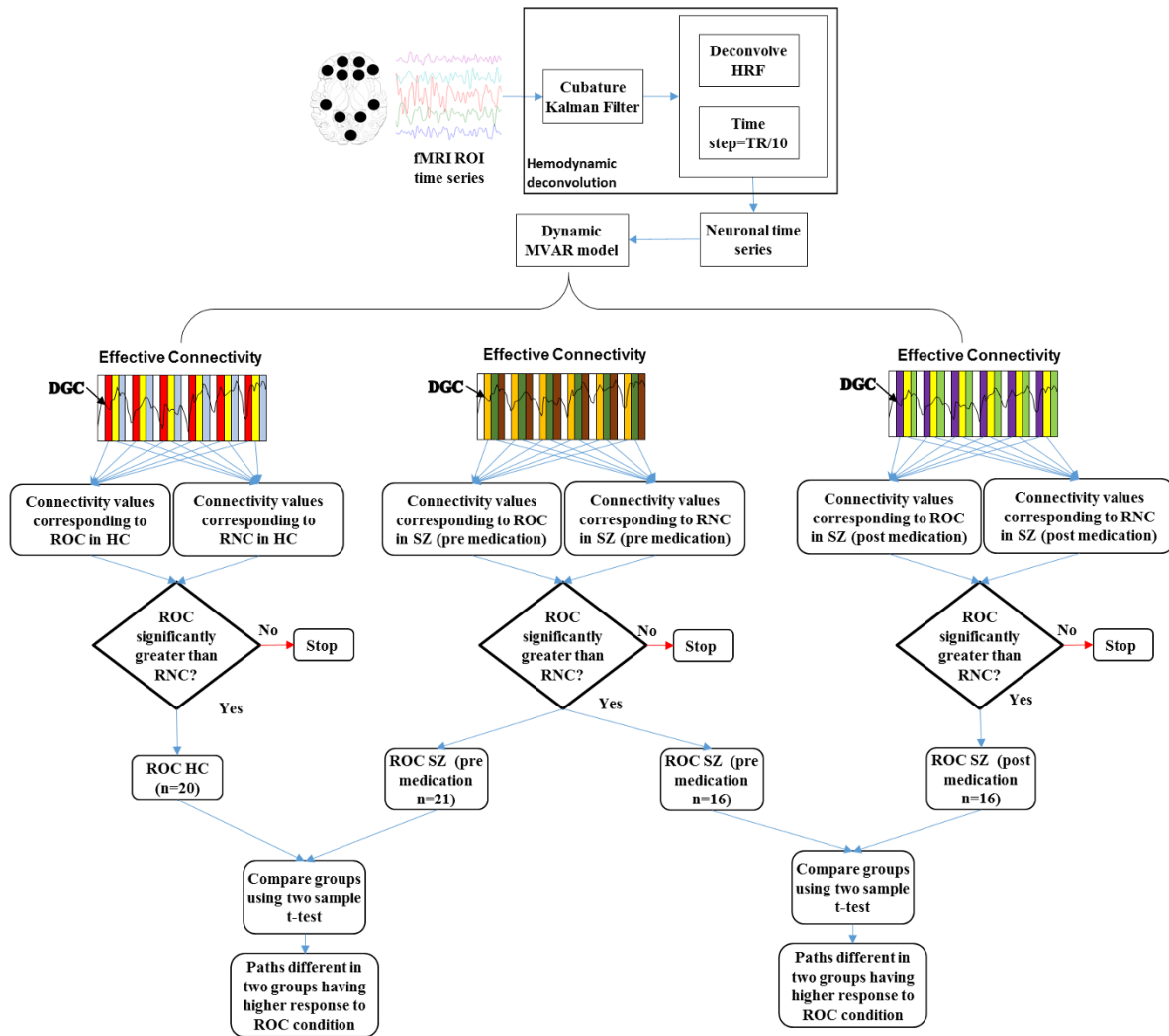


**Figure 4.12** Effective connectivity analysis schematic

### 4.4.3 Results

The between group analysis of HC and unmedicated SZ showed that healthy controls had more number of paths that had greater ROC – RNC activation and were significantly stronger when compared to the unmedicated SZ group (figure 4.13). Between-group analysis of the SZ group showed that before medication the SZ group had a lesser number of paths that were significantly greater (unmedicated SZ > medicated SZ) (figure 4.14) when compared to participants after 1-week of medication. For both figures 4.13 and 4.14 (plotted using Gephi [99]) the frontal brain

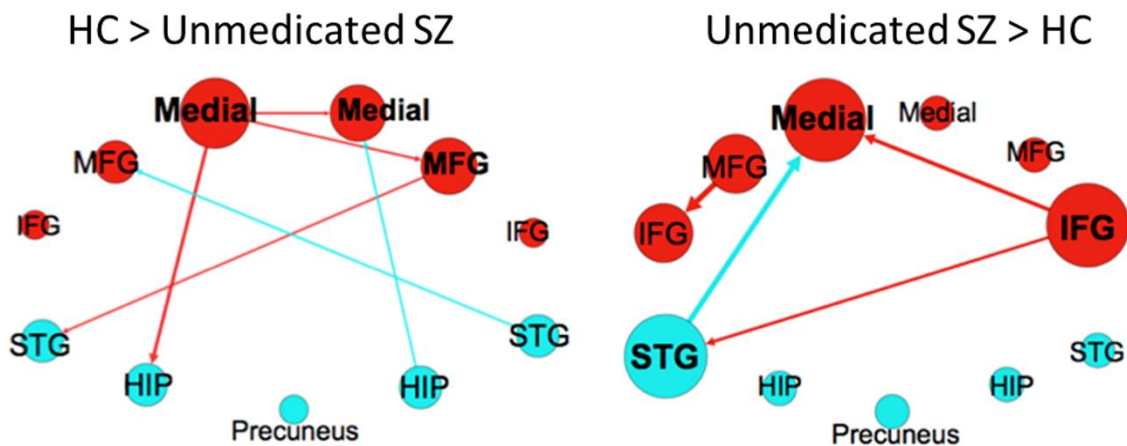


**Figure 4.13** Paths that were (left) significantly greater in healthy control than unmedicated schizophrenia (HC > SZ) (right) paths that were significantly greater in unmedicated schizophrenia compared to healthy controls (SZ > HC)

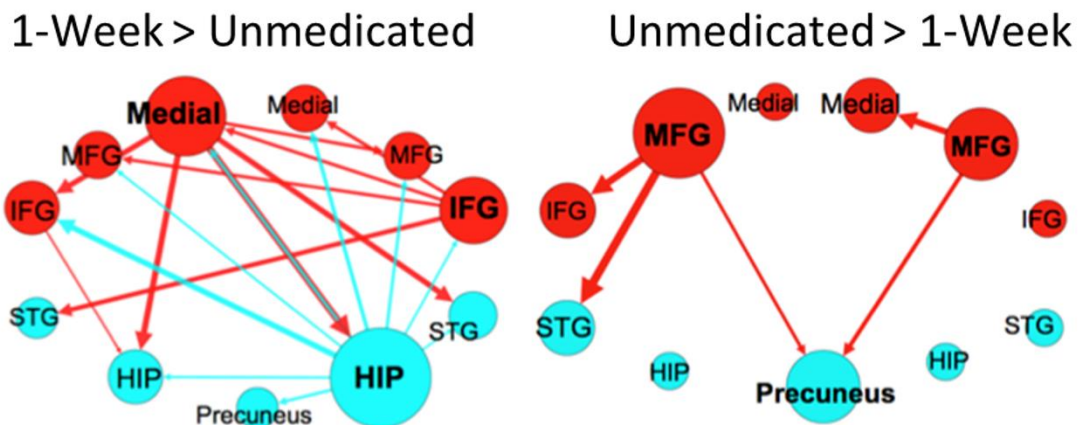


**Figure 4.14** Paths that were (left) significantly greater in patients with schizophrenia after medication (Medicated SZ > Unmedicated SZ) and (right) paths that were significantly greater before medication (Unmedicated SZ > Medicated).

regions are depicted in red and the posterior in blue with the size of the ROI circle and name corresponding to that region's degree (how many paths were originating from or projecting to that region). Paths with greater path weights are depicted as having thicker lines. Abbreviations are as follows: IFG, inferior frontal gyrus; Medial, medial frontal gyrus; MFG, middle frontal gyrus; HIP, posterior hippocampus; STG, superior temporal gyrus. ROIs are arranged as if looking on top of head from above with left side on the left half and right side on right half of the figure.

#### **4.4.4 Discussion**

In conclusion, we found that patients with schizophrenia show deficits in the memory network when compared with healthy control subjects. We also found that the memory network in schizophrenia shows increased connectivity after 1-week of treatment. These data further our knowledge of the disruptions within the memory network in schizophrenia and how this network responds to antipsychotic therapy. In addition these findings indicate that effective connectivity techniques utilizing fMRI can be very useful in probing the functioning of the memory network in schizophrenia.

#### **4.5 Effective connectivity analysis of visual-motor network in patients with schizophrenia**

This study was done in collaboration with Nathan Hutcheson, Mina Hanna, David White and Dr. Adrienne Lahti. All the above mentioned collaborators are from the University of Alabama - Birmingham, Birmingham, AL. My main contributions to this paper are effective connectivity analysis of the data and helping write the paper, under the guidance of Dr. Gopikrishna Deshpande.

### **4.5.1 Introduction**

Previous work has shown that EC can be used to map connections between brain areas in auditory motor tasks in healthy controls (HC) [24]. Previous work in schizophrenia has shown low-level abnormalities in perceptual processing of visual stimuli [100] and also motor function [101]. Although there is information about altered functional connectivity in the visuo-motor pathway, the directionality of the altered connections, which is critical given the known causal flow of information between visual and motor cortices, is unknown. In our current study, we have used fMRI to study the EC between visual and motor cortices in HC and patients with schizophrenia (SZ). We investigated if there was altered connectivity of paths originating from the visual cortex and projecting to motor areas in schizophrenia participants compared to the healthy controls.

### **4.5.2 Materials and Methods**

Functional magnetic resonance imaging (fMRI) data was collected on a 3T head-only (Siemens Allegra) scanner in 21 off-medication SZ and 20 healthy control (HC) subjects. During the performance of the fMRI task, subjects were shown a series of words and after each, asked to press a button with their left or right index finger to indicate if the word was novel or previously seen. The functional data were acquired using the gradient recalled echo-planar imaging (EPI) sequence (TR/TE/flip angle/FOV/slice thickness = 2100ms/30ms/70°/24cm/4mm). All data were preprocessed using SPM 8. Five regions of interest (ROI) were chosen based on the activation maps and the mean percent signal change time series were extracted and input to the dynamic connectivity model discussed in chapter-3 to obtain DGC measures. The mean time series were temporally normalized and deconvolved using a CKF [32] and input into a dMVAR model [31, 45, 91] to obtain connectivity between every pair of ROIs as a function of time. Based on the

causal connectivity values we obtained the dominant directional influence score for each path. For example, if the connectivity strength of a path from ROI A to ROI B is greater than ROI B to ROI A, then the path ROI A to ROI B will be assigned an influence score of (path weight of ROI A to ROI B) - (path weight of ROI B to ROI A) and the influence score of path ROI B to ROI A will be set to (path weight of ROI B to ROI A) - (path weight of ROI A to ROI B). The obtained influence scores during the task of interest (when the participant gave a correct answer) were then populated into different samples for both HC and SZ participants separately. Then a right tailed t-test was performed on the sample to obtain the paths that were significantly ( $p < 0.05$ ) greater than zero for both the groups (HC and SZ). A two sample t-test was also done between these samples to find paths that were significantly different between the two groups (SZ and HC). These paths

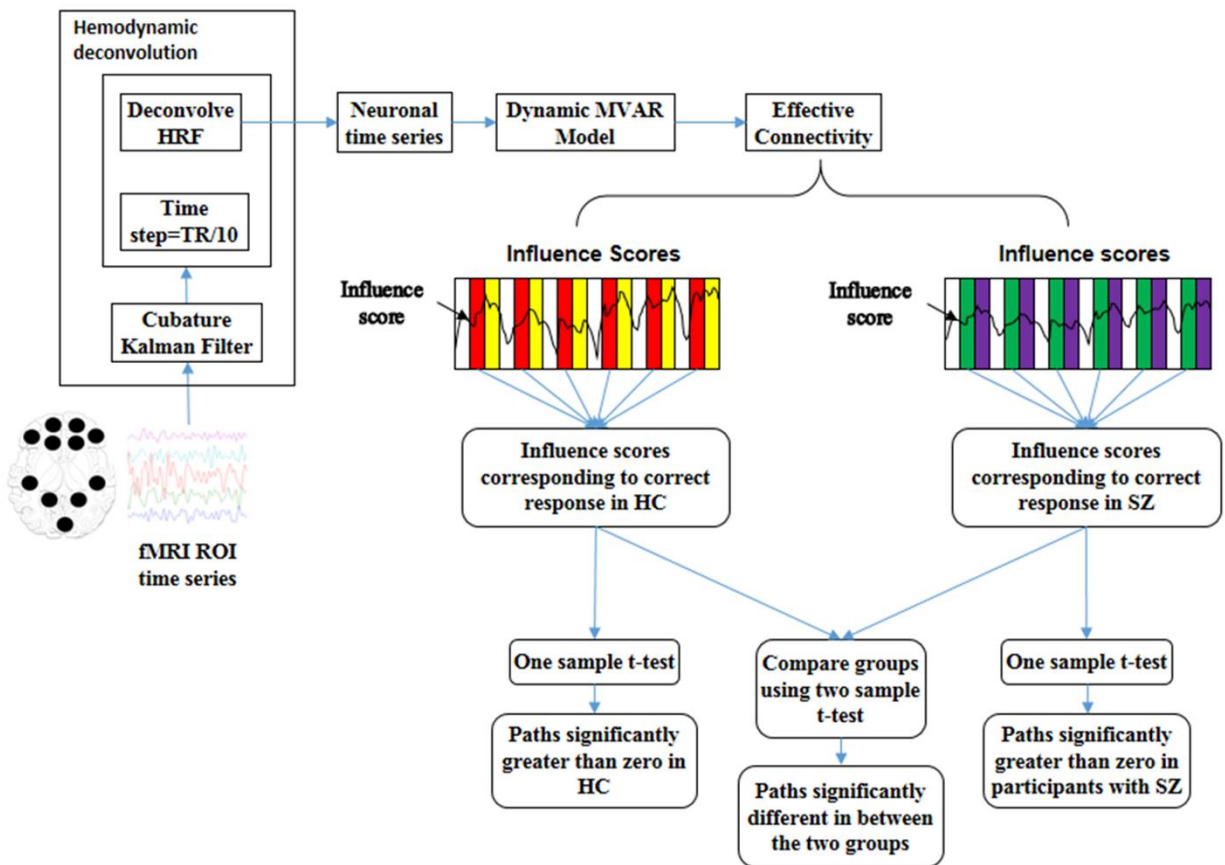


**Figure 4.15** Effective connectivity analysis schematic

were illustrated by using the brainnet viewer toolbox [85]. Schematic of the connectivity analysis is given in figure 4.15.

### 4.5.3 Results

Figure 4.16 shows the paths that were significantly greater than zero for both HC and SZ participants. We found that, HC did show strong unidirectional connections that originated from the calcarine sulcus and projected to the bilateral precentral gyrus (PreCG) and bilateral supplementary motor areas (SMA). However, SZ participants showed less robust projections from calcarine sulcus to bilateral PreCG and SMA.

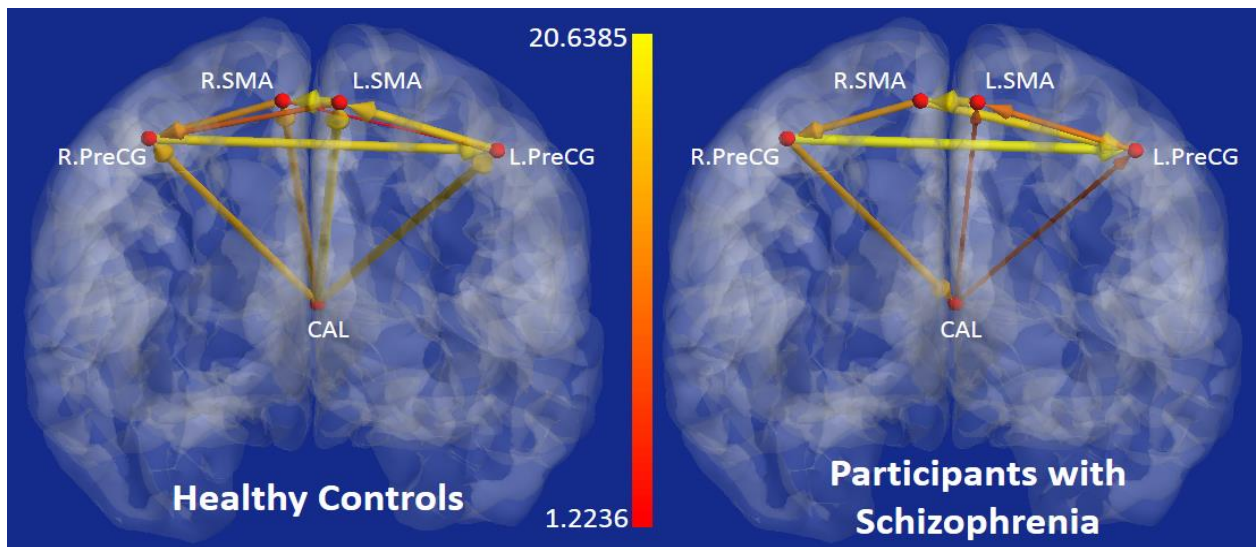


**Figure 4.16** Paths that were significant within the visual-motor network in healthy controls (n=20) and unmedicated patients with schizophrenia (n=21). Colorbar indicates the t-values.

When the HC and unmedicated SZ groups were contrasted, we found that the HC group had a significantly stronger projection from the calcarine sulcus toward the left and right precentral gyrus

and left and right SMA (figure 4.17). In contrast, the SZ group showed a stronger projection from the right precentral gyrus backward toward the calcarine sulcus.

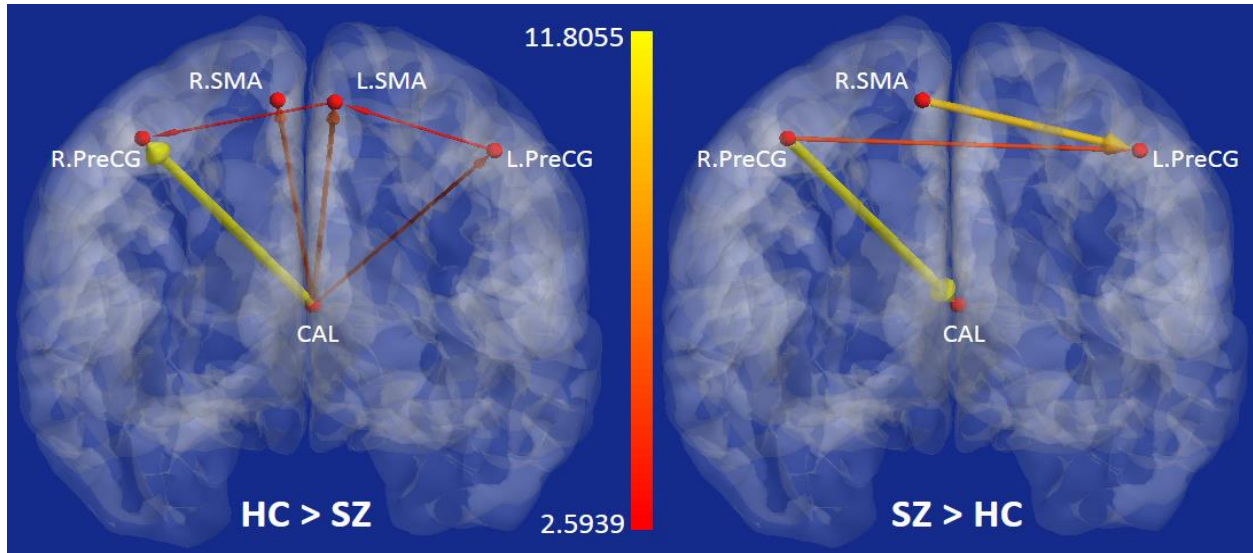


**Figure 4.17** Paths that were significantly greater within the visual-motor network in (left panel) healthy controls (n=20) compared to unmedicated patients with schizophrenia (n=21) (right panel) unmedicated patients with schizophrenia (n=21) compared to healthy controls (n=20). Colorbar indicates the t-values.

#### 4.5.4 Discussion

These results were consistent with previous work showing that in a visual-motor task, neural information proceeds from visual cortex to motor and supplementary motor areas [24]. Also, it shows a novel finding that the visual-motor deficits seen in schizophrenia may stem from altered connectivity within and between these networks. The effective connectivity method utilized was able to map connectivity within the visual-motor system in healthy controls and patients with schizophrenia. Also, this work showed that patients with schizophrenia have low-level disruption of visual-motor connectivity, which adds to a growing body of literature that schizophrenia is characterized by disrupted connectivity within multiple neural networks, some which are not traditionally associated with Schizophrenia.

## **4.6 Spatial imagery in haptic shape perception**

This study was done in collaboration with Dr. Simon Lacey, Dr. Randall Stilla and Dr. K. Sathian. All the above mentioned collaborators are from Emory University, Atlanta, GA. This work is submitted to *Neuropsychologia*. My main contributions to this work are effective connectivity analysis of the data and help write the paper, under the guidance of Dr. Gopikrishna Deshpande.

### **4.6.1 Introduction**

In an earlier study *Lacey et.al.* [102] proposed that haptic activation of the visually shape-selective lateral occipital complex (LOC) reflects a model of multisensory object representation in which the role of visual imagery is modulated by object familiarity. Supporting this model, a visual object imagery [103] task produced more similar patterns of effective connectivity, with haptic perception of familiar, than unfamiliar, shape [47]. In this current study, we test the hypothesis that a visual spatial imagery (spIMG) [103] task would more similar effective connectivity networks, with haptic perception of unfamiliar shape (uHS) than familiar shape (fHS).

### **4.6.2 Materials and Methods**

fMRI data was acquired on a 3 Tesla Siemens Trio whole body scanner (Siemens Medical Solutions, Malvern, PA) from twelve neurologically normal participants (TR/TE/flip angle/FOV/slice thickness = 2000ms/30ms/90°/220mm/4mm). The volunteers performed spIMG, uHS and fHS tasks in two fMRI sessions. During the spIMG task participants memorize lettered 4x4 grid and in response to auditory four-letter strings, participants imagine the shape resulting from filling in the appropriate squares. The control task was to decide whether a four-letter string made a real word or non-word. During the haptic task the participants were presented with a series of objects

and performed a one-back same/different shape discrimination. During the uHS task unfamiliar objects (meaningless wooden blocks) were the shape stimuli while for fHS familiar objects (rubber duck, spoon, etc.) were the shape stimuli. The control condition was a one-back same/different texture discrimination. fMRI time series were extracted from 31 ROIs for all participants and DGC values obtained using the dynamic connectivity model described in chapter-3. The hidden neuronal variables were obtained by hemodynamic blind deconvolution of the normalized mean time series [32], and were input into a dMVAR model [31, 45, 91] to obtain the connectivity estimates. The DGC metrics obtained across all the participants were populated in different samples corresponding to the imagery task performed (uHS, fHS or SPIM) and corresponding control conditions and t-tests were performed between the condition-specific samples and paths significantly greater during the imagery tasks were obtained. From these significant paths those which are common between SPIM & uHS perception tasks and the SPIM & fHS perception tasks were obtained. A two dimensional correlation was done between the thresholded ( $p < 0.05$ ) mean connectivities of different imagery tasks. The analysis pipeline is shown in figure 4.18.

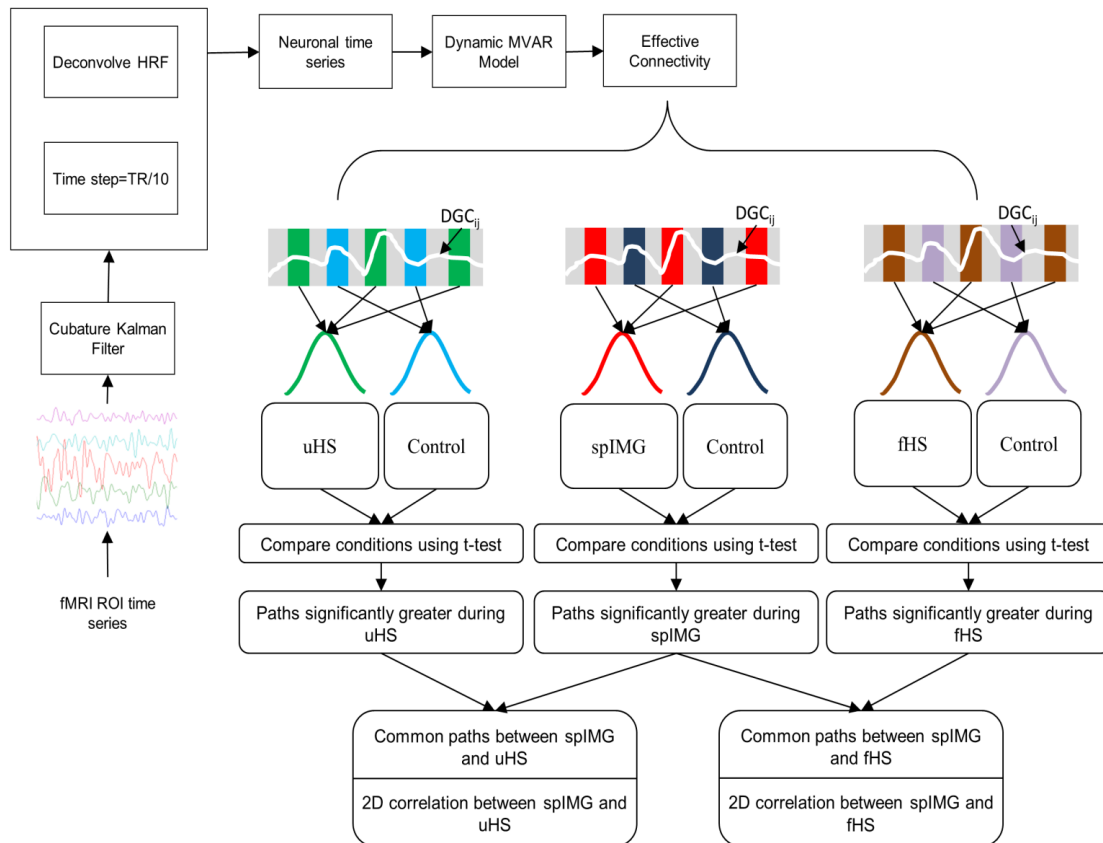


**Figure 4.18** Effective connectivity analysis pipeline

### 4.6.3 Results

Figure 4.19 shows the paths which were significantly stronger during both the spIMG and fHS tasks as compared to their respective control tasks while figure 4.20 shows the same for the spIMG and uHS tasks. From these figures we can see that there are more significant paths that were common between spIMG and uHS when compared to the number of common paths between spIMG and fHS.

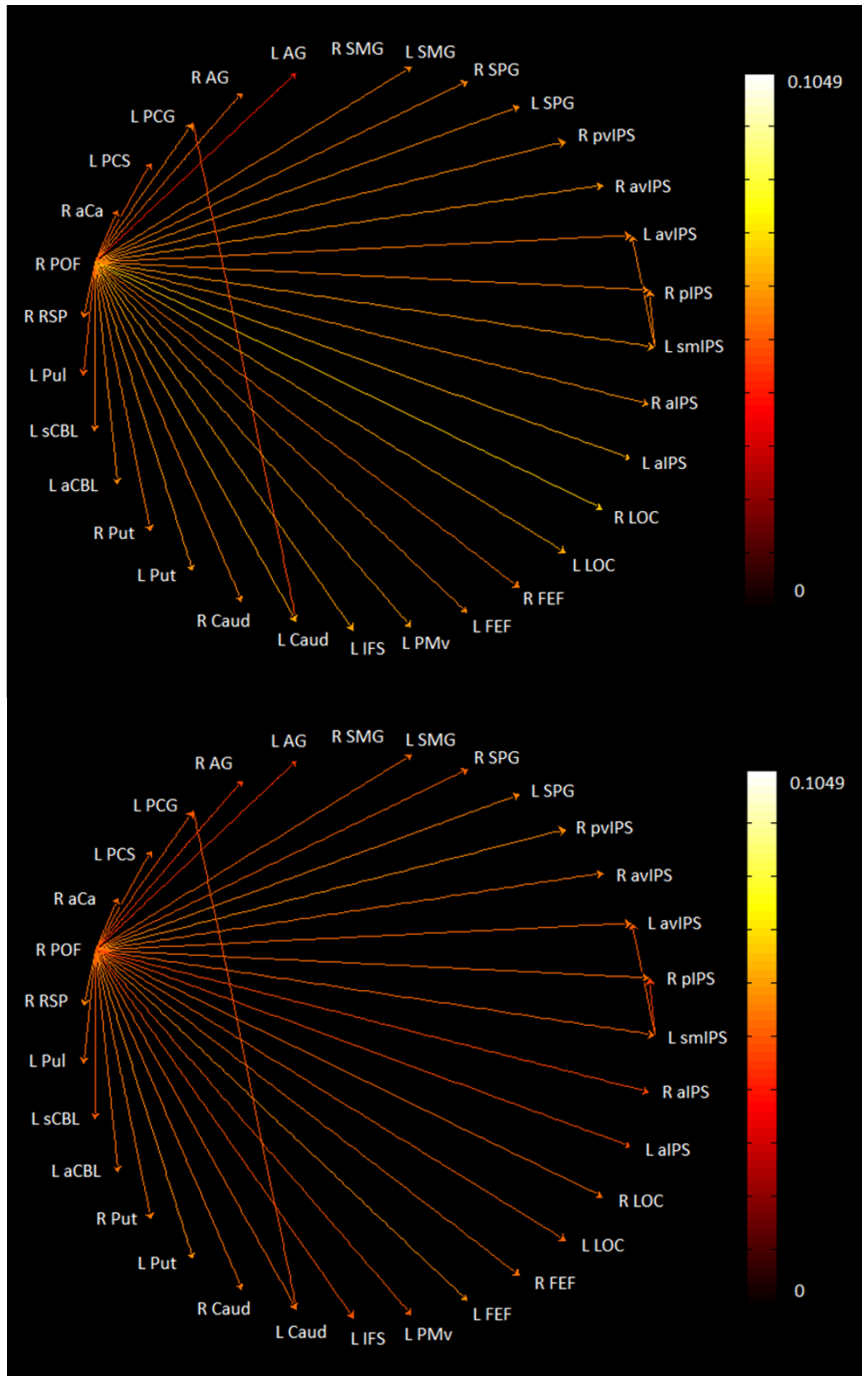


**Figure 4.19** Paths which were significantly stronger during both spIMG and fHS tasks as compared to the control task: a) (top) edge color represented by spIMG task path weight; b) (bottom) edge color represented by fHS perception task path weight.

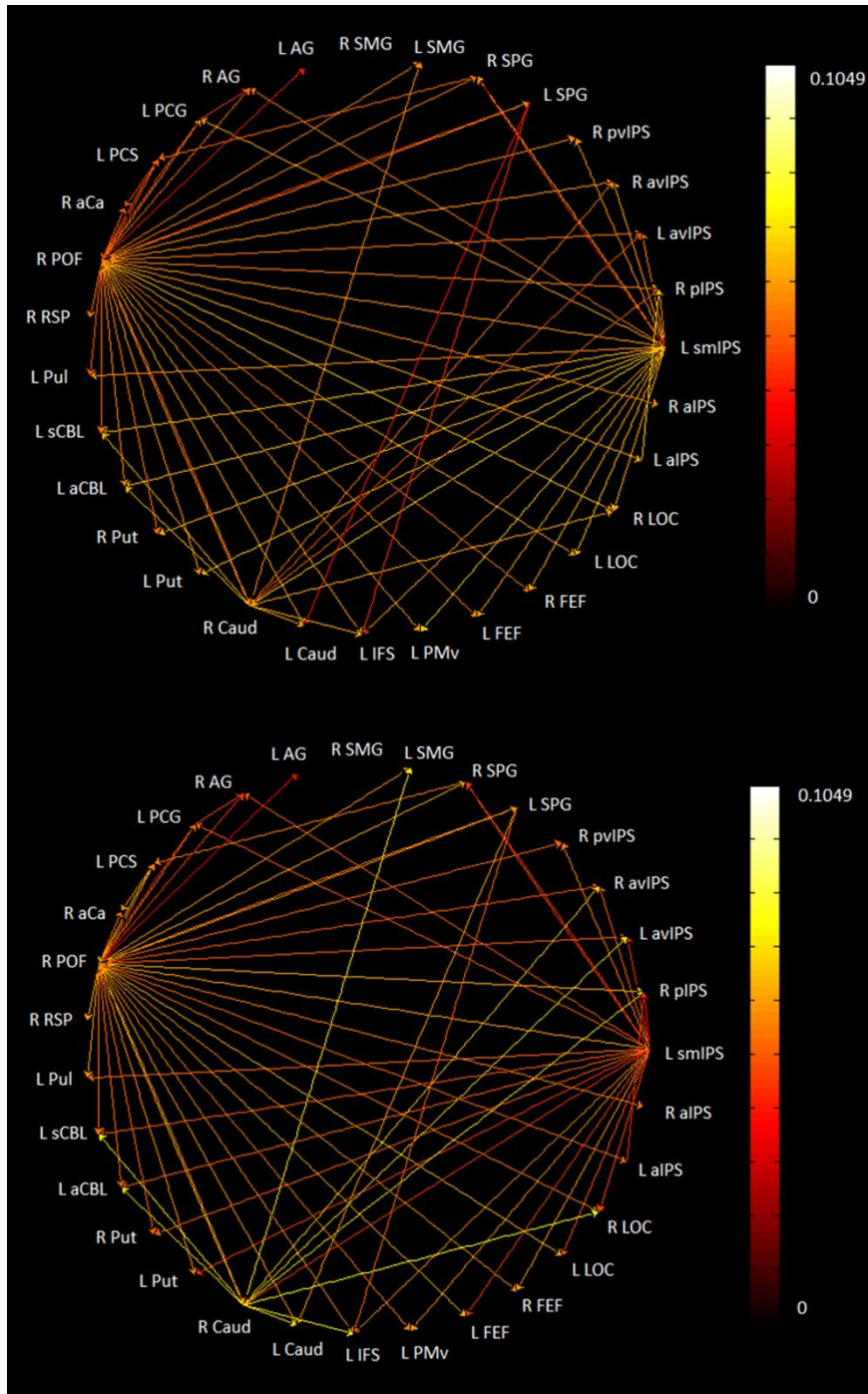


**Figure 4.20** Paths which were significantly stronger during both spIMG and uHS tasks as compared to the control task: a) (top) edge color represented by spIMG task path weights; b) (bottom) edge color represented by uHS task path weights.

Two dimensional correlations were performed using the thresholded ( $p < 0.05$ ) connectivity matrices between the above mentioned pairs (spIMG & uHS, spIMG & fHS). The spIMG and uHS

task connectivities were significantly correlated ( $r=0.25$ ,  $p= 5.89\times 10^{-15}$ ), whereas the correlation between the spIMG and fHS tasks was not significant ( $r=0.03$ ,  $p= 0.32$ ). Figure 4.21 shows the

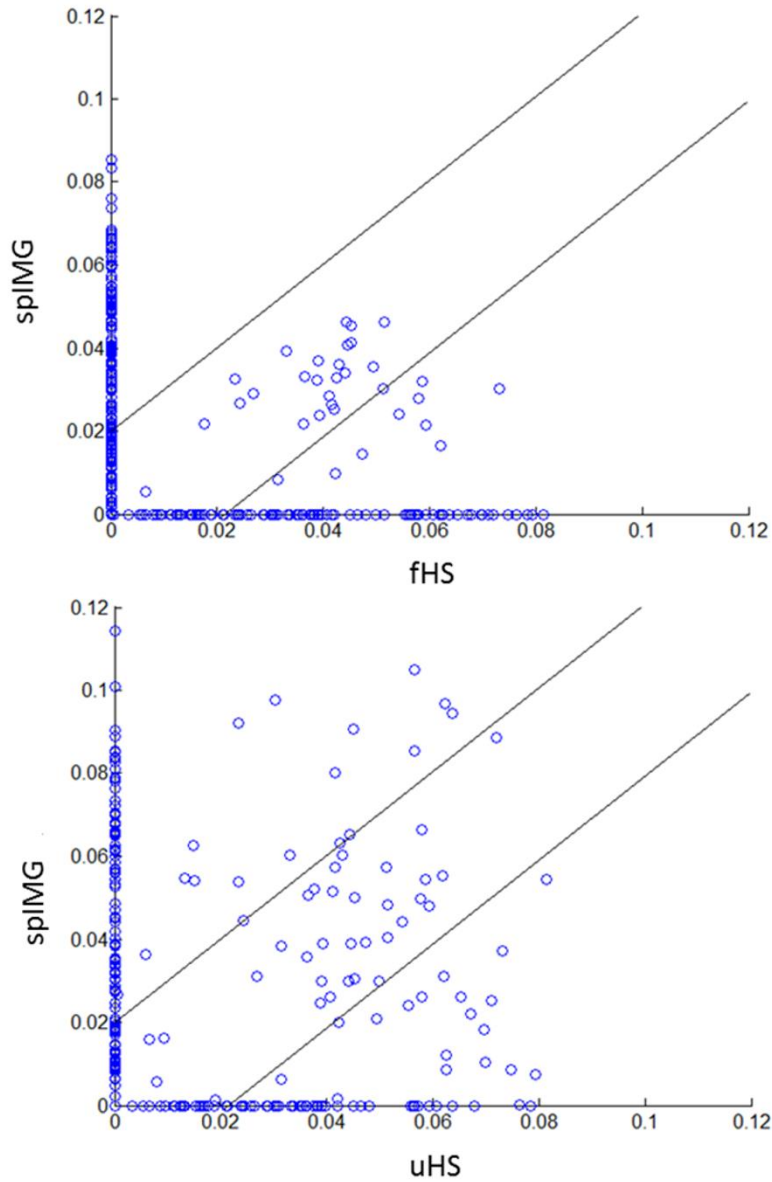


**Figure 4.21** Scatter plot illustrating the comparison between significant paths for spIMG and fHS (top) and uHS (bottom). The blue circles indicate different paths that were significantly greater during the task of interest when compared to the control condition. The circles on the  $x$  and  $y$  axes are paths that were not significant in one task but significant in the other. The circles that lie between the two axes are paths which were significant in both the tasks. The paths close to the line oriented at  $45^\circ$  angle on the scatter plot are significant in both tasks and also have very similar connectivity weights.

scatter plot illustrating the relationship between the weights of significant paths for spIMG & uHS as well as spIMG & fHS. These scatter plots were generated based on the thresholded ( $p < 0.05$ ) connectivity matrices for the respective imaging tasks. We can see from these plots that there are more significant paths that are common in the SPIM and uHS perception task when compared to the SPIM and fHS perception task comparison

#### **4.6.4 Discussion**

We can summarize our findings as follows a) The effective connectivity analysis showed that there were more paths significantly greater during imaging task that were common between SPIM and uHS when compared to number of common paths between SPIM and fHS perception tasks. b) 2D correlation between the spIMG and uHS effective connectivity networks were significant and positive while the spIMG and fHS networks were non-significantly correlated. Thus based on these findings we can say that the effective connectivity analyses were consistent with our proposed model, supporting a stronger relation between spatial imagery and haptic perception of unfamiliar compared to familiar shapes.

#### **4.7 Effective connectivity among three large-scale networks in schizophrenia and bipolar disorder with psychosis**

This study was done in collaboration with Dr. Lena Palaniyappan, Dr. Sarina Iwabuchi and Dr. Peter Liddle. All of the above mentioned collaborators are from the University of Nottingham, Nottingham, UK. This work will be submitted to the Journal of the American Medical Association (JAMA) Psychiatry. My main contributions to this paper are effective connectivity analysis of the data and help write the paper, under the guidance of Dr. Gopikrishna Deshpande.

### **4.7.1 Introduction**

The two major psychotic disorders, schizophrenia and bipolar disorder with psychosis, display more shared than unique abnormalities in brain structure [104], function [105] and candidate genetic loci [106, 107]. Despite this similarity, the clinical course and functional outcome of these disorders are notably divergent [108, 109]. The early conceptualization of schizophrenia placed emphasis on certain features (the predominance of poor functional outcome, the absence of clearly defined periods of complete remission, and the presence of thought disorder (loosening of associations)) as cardinal to define its distinctive phenotype [110]. Clarifying the neuroanatomical basis of the distinction between these two disorders can greatly enhance our understanding of the pathophysiological core of schizophrenia. Thus in this study we compared the EC using a triple network model (involving the default mode network, salience network and central executive network) in patients with schizophrenia and psychotic bipolar disorder to establish the diagnostic classification accuracy that can be achieved using this model.

### **4.7.2 Materials and Methods**

The sample consisted of 38 patients satisfying DSM-IV criteria for schizophrenia or schizoaffective disorder and 19 subjects with psychotic bipolar disorder. Functional MRI images were acquired on a 3 Tesla Philips Achieva MRI scanner (dual-echo EPI, 8ch SENSE, TR=2500ms, TE1/TE2 = 25/53ms, flip angle = 85°, FOV = 255 mm, slice thickness = 4mm) during 10 minutes of rest, with eyes open. Eight ROIs corresponding to three resting networks (default mode – ventromedial prefrontal cortex [vMPFC] and posterior cingulate cortex [PCC]; salience network – right and left anterior fronto-insular cortex [FIC] and dorsal anterior cingulate [ACC]; central executive network CEN – right and left posterior parietal [PPC] and right dorsolateral

prefrontal [DLPFC]) were based on the nodes reported by Shridaran *et. al* [21]. The mean time series from 8 ROIs were obtained for each of the 57 participants (19 Bipolar and 38 Schizophrenia participants) and the CPGC values were obtained using the static connectivity model shown in the previous chapter. First, the extracted time series were normalized and deconvolved using the CKF method [32] to obtain the underlying latent neuronal variables, which were then input into the MVAR model [47, 79] to obtain the granger causal metrics between the 8 ROIs for all the participants. For each possible path between the 8 ROIs, a t-test was performed between Schizophrenia and the Bipolar groups and those paths significantly different ( $p < 0.05$ ) between the groups were obtained. The granger causal measures obtained and the standardized clinical interview (SSPI) scores on reality distortion, disorganization, and psychomotor poverty for all the 57 participants were input into two different RCE-SVM classifiers [84] to determine the top features that helped the classifier predict the group membership of the subject (Schizophrenia or Bipolar) with maximum accuracy.

### **4.7.3 Results**

The classifier for triple network effective connectivity attained a maximum classification accuracy of 82.5% (sensitivity = 80.4%; specificity = 90.9%;  $p$ -value =  $3.76 \times 10^{-07}$ ) using 19 feature clusters comprising of 37 effective connectivity paths. We set out to investigate those paths which were statistically separated, i.e significantly ( $p < 0.05$ ) different between the two groups, as well as important for classification, i.e. among the 37 highest ranked features responsible for maximum classification accuracy. Such paths are illustrated in figure 4.22 (visualized using the BrainNet viewer toolbox [85]). It demonstrates reduced cross network connectivity in schizophrenia subjects compared to the bipolar subjects. The causal interactions were reduced in the schizophrenia subjects even when there was no task stimulus given to the subjects.

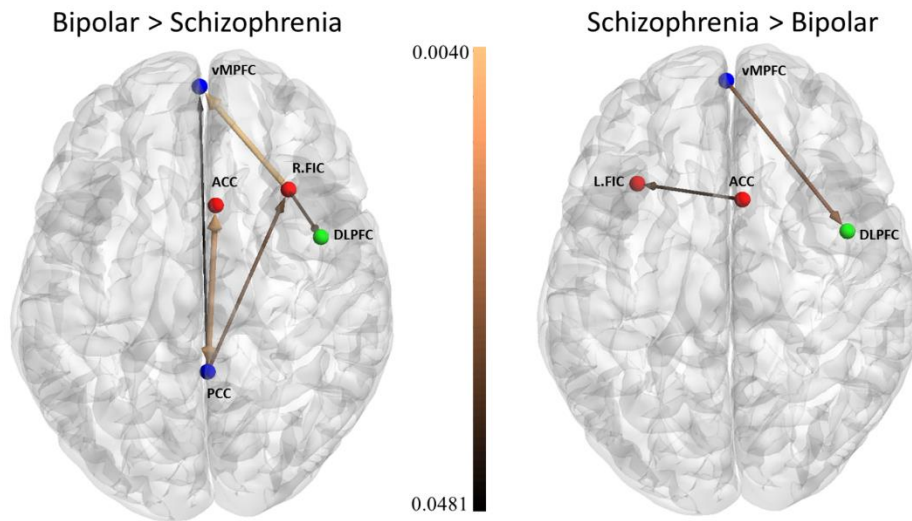


**Figure 4.22** (left) Paths significantly stronger in bipolar participants compared to schizophrenia participants. (right) Paths significantly stronger in schizophrenia participants compared to bipolar participants. The color of the node indicates the network the ROI belongs to: Blue – Default mode network; Red – Salience network; Green – Central executive network. The color and width of the paths indicate the p-value of the between group comparison

The classification analysis using the behavior scores of reality distortion, disorganization, and psychomotor poverty resulted in a maximum classification accuracy of 66.7% ( $p$ -value=0.0082) using all the three features. The disorganization score was the most discriminative feature for classification between the schizophrenia and bipolar participants (based on SVM score) followed by psychomotor poverty and reality distortion.

#### 4.7.4 Discussion

A high level of classification accuracy (82.5%) was achieved using the effective connectivity profiles of the three networks when discriminating patients with schizophrenia from those with bipolar disorder. This accuracy was superior to the 66.7% accuracy achieved using symptom clusters alone. From the results we can also see that, when compared to patients with bipolar disorder, patients with schizophrenia displayed a pattern of connectivity that indicated a significant reduction in the interaction among the triple networks. The most significant differences involved

the influence from salience network to the default mode network (rFIC to vMPFC and ACC to PCC), which was reduced in patients with schizophrenia when compared to patients with bipolar disorder. Further, among the 8 effective connectivity measures that were different between the two groups, 6 of them represented between or internetwork interactions while only 2 represented within or intra-network interactions. Therefore these results support the view that the study of network-level connectivity patterns can not only clarify the pathophysiology of schizophrenia but also provide a measure of incremental clinical utility in identifying discrete diagnostic/prognostic groups among individuals with psychosis.

## Chapter 5 Conclusion

In this thesis we have discussed, a) A non-parametric method for hemodynamic deconvolution and b) An effective connectivity model using the granger causality method. It is a well-known fact that the Functional MRI (fMRI) is a Blood Oxidation Level Dependent (BOLD) technique which does not directly measure neuronal activity and is assumed to be the linear convolution of latent neuronal response and the Hemodynamic Response Function (HRF). Since the main interest of any study would be to study the neuronal response, it is advantageous to deconvolve the HRF from the fMRI signal. In chapter-2 we presented a new non-parametric deconvolution method to perform hemodynamic deconvolution of the fMRI signal and compared its performance with already existing parametric method based on cubature Kalman filter. We postulated that if the performance of these two methods (non-parametric and parametric methods) were similar then we can ignore the problem of over fitting for highly parameterized models. We tested this hypothesis by deconvolving simulated as well as experimental fMRI signals using both non-parametric and parametric methods. The comparison of performance of these two methods showed that they performed very well, and in both cases the temporal neuronal events were correctly estimated. Based on similar performance of the two methods, and the fact that homomorphic method is a non-parametric method that does not make any assumptions we confirmed that the parametric methods such as cubature Kalman filter-based approaches make valid assumptions and are not susceptible to over-fitting.

In chapter-3 we presented the EC model based on principle of granger causality (GC). One major concern related to EC studies implementing GC analysis is the non-neuronal spatial variability of the hemodynamic response confounding results of the analysis. In our proposed model we addressed this issue by first performing hemodynamic deconvolution of the fMRI data to obtain the latent neuronal response and then apply the MVAR model to obtain the causal connectivity metrics. In the fourth chapter we demonstrated the utility of this EC model (described in chapter-3) by applying it to perform EC analysis of various fMRI data sets. The first study described in chapter-4 was a task based experiment to study connectivity in Autism spectrum disorder. We applied our model to investigate the EC in a theory of mind study in high functioning adults with autism. We also performed a classification analysis using the Recursive cluster elimination based support vector machine (RCE-SVM) on various metrics (functional connectivity, effective connectivity, behavioral scores and fractional anisotropy obtained from DTI data) for each participant as features to determine the accuracy with which the two groups (autism and controls) can be classified. We found that the EC was significantly reduced in participants with autism compared to controls. In addition to this the EC paths weights were the most important features in classification and were successfully able to classify the two groups with a very high accuracy. The second study discussed was related to major depression disorder (MDD), the GC model was used to investigate whether differential amygdala reactivity within MDD based on early life stress history was associated with failure of inhibition from medial or lateral PFC. We obtained results that supported our hypothesis. In the third study we analyzed the fMRI data set obtained from an experiment based on fear conditioning, we examined the EC in the brain in response to predictable and unpredictable unconditioned stimulus presentations in healthy controls by applying our EC model. The results of this study were in agreement with earlier findings and provided further

insights related to the causal connectivity in the brain related to fear conditioning. The fourth and fifth studies discussed in chapter-4 investigated EC in Schizophrenia. In the fourth study EC analysis was performed between brain regions that underlie episodic memory in healthy controls and participants with schizophrenia (before and after medication). In the fifth study we performed EC analysis to investigate if there was altered connectivity in the visual-motor network in schizophrenia participants compared to the healthy controls. The main findings of the study involving the memory network showed that patients with schizophrenia show weaker connectivity strength in the memory network when compared with healthy control subjects and the connectivity between the regions improved after treatment. In the study involving the visual-motor network we showed that visual-motor deficits seen in schizophrenia may stem from altered connectivity within and between the visual and motor networks and also showed that participants with schizophrenia had low-level disruption of connectivity between these two networks. In the sixth study discussed in chapter-4, we test the hypothesis that a visual spatial imagery task would produce more similar EC networks with haptic perception of unfamiliar shape than familiar shape. The results were in agreement with our hypothesis and as proposed there was a more similar connectivity in regions involved in spatial imagery and haptic perception of unfamiliar compared to familiar shapes. The final study in chapter-4 analyzes resting state fMRI data obtained from participants with schizophrenia and bipolar disorder. We input the EC measures obtained using our GC model and behavioral measures to distinguish between participants with schizophrenia and those with bipolar disorder by using an RCE-SVM classifier. We found that the EC measures performed better in classifying the two groups and also found that there was significant reduction in the interaction among the default mode network, salience network and central executive network in participants with SZ compared to participants with bipolar disorder.

## Bibliography

- [1] E. M. Purcell, H. C. Torrey and R. V. Pound, "Resonance Absorption by Nuclear Magnetic Moments in a Solid," *Physical Review*, vol. 69, pp. 37-38, 1946.
- [2] F. Bloch, W. W. Hansen and M. Packard, "Nuclear Induction," *Physical Review*, vol. 69, p. 127, 1946.
- [3] E. M. Haacke, R. F. Brown, M. Thompson and R. Venkatesan, *Magnetic resonance imaging: Physical principles and sequence design*, New York: J. Wiley & Sons, 1999.
- [4] S. Ogawa, T. M. Lee, A. R. Kay and D. W. Tank, "Brain magnetic resonance imaging with contrast dependent on blood oxygenation," *Proceedings of the National Academy of Sciences USA*, vol. 87, pp. 9868-9872, 1990.
- [5] L. Pauling and C. D. Coryell, "The Magnetic Properties and Structure of Hemoglobin, Oxyhemoglobin and Carbonmonoxyhemoglobin," *Proceedings of the National Academy of Sciences USA*, vol. 22, p. 210-216, 1936.
- [6] S. A. Huettel, A. W. Song and G. McCarthy, *Functional Magnetic Resonance Imaging*, Sinauer Associates, Incorporated, 2009.
- [7] K. J. Friston, P. Jezzard and R. Turner, "Analysis of functional MRI time series," *Human Brain Mapping*, vol. 2, pp. 69-78, 1994.
- [8] E. Kandel, J. Schwartz and T. Jessel, *Principles of Neural Science*, 4 ed., New York: McGraw-Hill Companies, Inc, 2000.
- [9] F. Russo, A. Martinez, M. Sereno, S. Pitzalis and S. Hillyard, "Cortical sources of the early components of the visual evoked potential," *Human Brain Mapping*, vol. 15, pp. 95-111, 2001.
- [10] B. Sadeh, A. Zhdanov, I. Podlipsky, T. Hendler and G. Yovel, "The validity of the face-selective ERP N170 component during simultaneous recording with functional MRI," *NeuroImage*, vol. 42, pp. 778-786, 2008.
- [11] P. Sauseng and W. Klimesch, "What does phase information of oscillatory brain activity tell us about cognitive processes?," *Neuroscience & Biobehavioral Reviews*, vol. 32, pp. 1001-1013, 2008.
- [12] K. J. Friston, "Functional and effective connectivity in neuroimaging: a synthesis," *Human Brain Mapping*, vol. 2, pp. 56-78, 1995.
- [13] B. Biswal, F. Yetkin, V. Haughton and J. Hyde, "Functional connectivity in the motor cortex of resting human brain using echo-planar MRI," *Magnetic Resonance in Medicine*, vol. 34, pp. 537-541, 1995.
- [14] J. O'Reilly, M. Woolrich, T. Behrens, S. Smith and H. Johansen-Berg, "Tools of the trade: psychophysiological interactions and functional connectivity," *Social Cognitive and Affective Neuroscience*, vol. 7, pp. 604-609, 2012.
- [15] G. Deshpande, S. LaConte, G. James, S. Peltier and X. Hu, "Multivariate Granger causality analysis of brain networks," *Human Brain Mapping*, vol. 30, pp. 1361-1373, 2009.

- [16] A. McIntosh and F. Gozales-Lima, "Structural equation modelling and its application to network analysis in functional brain imaging," *Human Brain Mapping*, vol. 2, pp. 2-22, 1994.
- [17] A. Roebroeck, E. Formisano and R. Goebel, "Mapping directed influence over the brain using Granger causality and fMRI," *NeuroImage*, vol. 25, pp. 230-242, 2005.
- [18] K. J. Friston, L. Harrison and W. Penny, "Dynamic causal modelling," *Neuroimage*, vol. 19, pp. 1273-1302, 2003.
- [19] G. Deshpande, P. Santhanam and X. Hu, "Instantaneous and causal connectivity in resting state brain networks derived from functional MRI data," *NeuroImage*, vol. 54, pp. 1043-1052, 2011.
- [20] W. Liao, D. Mantini, Z. Zhang, Z. Pan, J. Ding, Q. Gong, Y. Yang and H. Chen, "Evaluating the effective connectivity of resting state networks using conditional Granger causality," *Biological Cybernetics*, vol. 102, pp. 57-69, 2010.
- [21] D. Sridharan, D. Levitin and V. Menon, "A critical role for the right fronto-insular cortex in switching between central-executive and default-mode networks," *Proceedings of the National Academy of Sciences USA*, vol. 105, p. 12569–12574, 2008.
- [22] J. Zhuang, S. LaConte, S. Peltier, K. Zhang and X. Hu, "Connectivity exploration with structural equation modeling: an fMRI study of bimanual motor coordination," *NeuroImage*, vol. 25, pp. 462-470, 2005.
- [23] G. Deshpande, X. Hu, R. Stilla and K. Sathian, "Effective Connectivity during Haptic Perception: A study using Granger causality analysis of functional magnetic resonance imaging data," *NeuroImage*, vol. 40(4), pp. 1807-1814, 2008.
- [24] B. Abler, A. Roebroeck, R. Goebel, A. Hose, C. Schnfeldt-Lecuona, G. Hole and H. Walter, "Investigating directed influences between activated brain areas in a motor-response task using fMRI," *Magnetic Resonance Imaging*, pp. 24: 181-185, 2006.
- [25] K. Sathian, S. Lacey, R. Stilla, G. Gibson, G. Deshpande, X. Hu, S. LaConte and C. Glielmi, "Dual pathways for haptic and visual perception of spatial and texture information," *NeuroImage*, vol. 57, no. 2, pp. 462-475, 2011.
- [26] D. Handwerker, J. Ollinger and M. D'Esposito, "Variation of BOLD hemodynamic responses across subjects and brain regions and their effects on statistical analyses," *NeuroImage*, p. 21: 1639–1651, 2004.
- [27] G. Deshpande, K. Sathian and X. Hu, "Effect of hemodynamic variability on Granger causality analysis of fMRI," *NeuroImage*, vol. 52, no. 3, pp. 884-896, 2010.
- [28] O. David, I. Guillemain, S. Sallet, S. Reyt, C. Deransart, C. Segebarth and A. Depaulis, "Identifying Neural Drivers with Functional MRI: An Electrophysiological Validation," *PLoS Biology*, pp. 6(12): 2683-2697, 2008.
- [29] G. Deshpande, L. E. Libero, K. R. Sreenivasan, H. D. Deshpande and R. K. Kana, "Identification of neural connectivity signatures of autism using machine learning," *Frontiers in Human Neuroscience*, no. 7, p. 670, 2013.
- [30] S. Ryali, K. Supekar, T. Chen and V. Menon, "Multivariate dynamical systems models for estimating causal interactions in fMRI," *Neuroimage*, vol. 54, no. 2, pp. 807-823, 2011.

- [31] K. Sathian, G. Deshpande and R. Stilla, "Neural changes with tactile learning reflect decision-level reweighting of perceptual readout," *The Journal of Neuroscience*, vol. 33, pp. 5387-5398, 2013.
- [32] M. Havlicek, K. Friston, J. Jan, M. Brazdil and V. Calhoun, "Dynamic modeling of neuronal responses in fMRI using cubature Kalman filtering," *NeuroImage*, vol. 56, no. 4, pp. 2109-2128, 2011.
- [33] R. B. Buxton, K. Uludag, D. J. Dubowitz and T. T. Liu, "Modeling the hemodynamic response to brain activation," *Neuroimage*, vol. 23, pp. S220-S233, 2004.
- [34] G. S. Berns, A. W. Song and H. Mao, "Continuous functional magnetic resonance imaging reveals dynamic nonlinearities of "dose-response" curves for finger opposition," *Journal of Neuroscience*, vol. 19, pp. 1-6, 1999.
- [35] A. Mechelli, C. J. Price and K. J. Friston, "Nonlinear coupling between evoked rCBF and BOLD signals: a simulation study of hemodynamic responses," *NeuroImage*, vol. 14, pp. 862-872, 2001.
- [36] K. J. Friston, A. Mechelli, R. Turner and C. J. Price, "Nonlinear responses in fMRI: the Balloon model, Volterra kernels, and other hemodynamics," *NeuroImage*, vol. 12, pp. 466-477, 2000.
- [37] R. B. Buxton, E. C. Wong and L. R. Frank, "Dynamics of blood flow and oxygenation changes during brain activation: the balloon model," *Magnetic Resonance in Medicine*, vol. 39, pp. 855-864, 1998.
- [38] J. Mandeville, J. Marota, C. Ayata, G. Zaharchuk, M. Moskowitz, B. Rosen and R. Weisskoff, "Evidence of a cerebrovascular postarteriole windkessel with delayed compliance," *Journal of Cerebral Blood Flow & Metabolism*, vol. 19, pp. 679-689, 1999.
- [39] J. T. Webb, M. A. Ferguson, J. A. Nielsen and J. S. Anderson, "BOLD Granger Causality Reflects Vascular Anatomy," *PLoS ONE*, vol. 8, no. 12, p. e84279, 2013.
- [40] G. Deshpande and X. Hu, "Investigating Effective Brain Connectivity from fMRI Data Past Findings and Current Issues with Reference to Granger Causality Analysis," *Brain Connectivity*, vol. 2, no. 5, pp. 235-245, 2012.
- [41] G. Deshpande, K. Sathian, X. Hu and J. Buckhalt, "A rigorous approach for testing the constructionist hypotheses of brain function," *Behavioral and Brain Sciences*, pp. vol. 35(3), pp. 148, 2012.
- [42] M. Strenziok, F. Krueger, G. Deshpande, R. Lenroot, E. van der Meer and J. Grafman, "Fronto-Parietal Regulation of Media Violence Exposure in Adolescents: A Multi-Method Study," *Social Cognitive and Affective Neuroscience*, pp. vol. 5, pp. 22, 2011.
- [43] F. Preusse, E. Van der Meer, G. Deshpande, F. Krueger and I. Wartenburger, "Fluid intelligence allows flexible recruitment of the parieto-frontal network in analogical reasoning," *Frontiers in Human Neuroscience*, pp. vol. 5, pp. 22, 2011.
- [44] F. Krueger, S. Landgraf, E. Van der Meer, G. Deshpande and X. Hu, "Effective connectivity of the multiplication network: A functional MRI and multivariate Granger causality mapping study," *Human Brain Mapping*, pp. vol. 32(9), pp. 1419-1431, 2011.
- [45] S. Lacey, H. Hagtvedt, V. M. Patrick, A. Anderson, R. Stilla, G. Deshpande, X. Hu, J. R. Sato, S. Reddy and K. Sathian, "Art for reward's sake: Visual art recruits the ventral striatum," *NeuroImage*, pp. vol. 55(1), pp. 420-433, 2011.

- [46] B. Hampstead, A. Stringer, R. Stilla, G. Deshpande, X. Hu, A. Moore and K. Sathian, "Activation and effective connectivity changes following explicit memory training for face-name pairs in patients with mild cognitive impairment: A pilot study," *Neurorehabilitation and Neural Repair*, pp. vol. 25(3), pp. 210-222, 2011.
- [47] G. Deshpande, X. Hu, S. Lacey, R. Stilla and K. Sathian, "Object familiarity modulates effective connectivity during haptic shape perception," *NeuroImage*, pp. vol. 49(3), pp. 1991-2000, 2010.
- [48] A. Mechelli, C. J. Price, U. Noppeney and K. J. Friston, "A Dynamic Causal Modeling Study on Category Effects: Bottom-Up or Top-Down Mediation?," *Journal of Cognitive Neuroscience*, vol. 15, no. 7, pp. 925-934, 2003.
- [49] T. Bitan, J. R. Booth, J. Choy, D. D. Burman, D. R. Gitelman and M. M. Mesulam, "Shifts of effective connectivity within a language network during rhyming and spelling," *The Journal of Neuroscience*, vol. 25, no. 22, pp. 5397-5403, 2005.
- [50] A. P. Smith, K. E. Stephan, M. D. Rugg and R. J. Dolan, "Task and content modulate amygdala-hippocampal connectivity in emotional retrieval," *Neuron*, vol. 49, no. 4, pp. 631-638, 2006.
- [51] G. Bird, C. Catmur, G. Silani, C. Frith and U. Frith, "Attention does not modulate neural responses to social stimuli in autism spectrum disorders," *Neuroimage*, vol. 31, no. 4, pp. 1614-1624, 2006.
- [52] K. Bush and J. Cisler, "Decoding neural events from fMRI BOLD signal: a comparison of existing approaches and development of a new algorithm," *Magnetic Resonance Imaging*, vol. 31, no. 6, pp. 976-989, 2013.
- [53] C. C. Gaudes, N. Petridou, I. L. Dryden, L. Bai, S. T. Francis and P. A. Gowland, "Detection and characterization of single-trial fMRI bold responses: Paradigm free mapping," *Human Brain Mapping*, vol. 32, no. 9, p. 1400-1418, 2011.
- [54] C. C. Gaudes, N. Petridou, S. T. Francis, I. L. Dryden and P. A. Gowland, "Paradigm free mapping with sparse regression automatically detects single-trial functional magnetic resonance imaging blood oxygenation level dependent responses," *Human Brain Mapping*, vol. 34, no. 3, pp. 501-518, 2013.
- [55] L. Hernandez-Garcia and M. O. Ulfarsson, "Neuronal event detection in fMRI time series using iterative deconvolution techniques," *Magnetic Resonance Imaging*, vol. 29, no. 3, pp. 353-364, 2011.
- [56] F. I. Karahanoğlu, C. Caballero-Gaudes, F. Lazeyras and D. Van de Ville, "Total activation: fMRI deconvolution through spatio-temporal regularization," *NeuroImage*, vol. 73, pp. 121-134, 2013.
- [57] G. R. Wu, W. Liao, S. Stramaglia, J. R. Ding, H. Chen and D. Marinazzo, "A blind deconvolution approach to recover effective connectivity brain networks from resting state fMRI data," *Medical Image Analysis*, vol. 17, no. 3, pp. 365-374, 2013.
- [58] I. Khalidov, J. Fadili, F. Lazeyras, D. Van De Ville and M. Unser, "Activelets: Wavelets for sparse representation of hemodynamic responses," *Signal Processing*, vol. 91, no. 12, pp. 2810-2821, 2011.

- [59] A. M. Wink, H. Hoogduin and J. B. Roerdink, "Data-driven haemodynamic response function extraction using Fourier-wavelet regularised deconvolution," *BMC Medical Imaging*, vol. 8, p. 7, 2008.
- [60] G. H. Glover, "Deconvolution of impulse response in event-related BOLD fMRI," *NeuroImage*, vol. 9, no. 4, pp. 416-429, 1999.
- [61] K. J. Friston, "Bayesian Estimation of Dynamical Systems: An Application to fMRI," *NeuroImage*, vol. 16, no. 2, pp. 513-530, 2002.
- [62] W. D. Penny, Z. Ghahramani and K. J. Friston, "Bilinear dynamical systems," *Phil. Trans. R. Soc. B*, vol. 360, no. 1457, p. 983-993, 2005.
- [63] S. Makni, C. Beckmann, S. Smith and M. Woolrich, "Bayesian deconvolution of fMRI data using bilinear dynamical systems," *NeuroImage*, vol. 4, no. 1, pp. 1381-1396, 2008.
- [64] K. J. Friston, N. Trujillo-Barreto and J. Daunizeau, "DEM: a variational treatment of dynamic systems," *Neuroimage*, vol. 41, no. 3, pp. 849-885, 2008.
- [65] J. J. Riera, J. Watanabe, I. Kazuki, M. Naoki, E. Aubert, T. Ozaki and R. Kawashima, "A state-space model of the hemodynamic approach: nonlinear filtering of BOLD signals," *Neuroimage*, vol. 21, no. 2, pp. 547-567, 2004.
- [66] A. V. Oppenheim and R. W. Schafer, "Homomorphic analysis of speech," *Audio and Electroacoustics, IEEE Transactions on*, vol. 16, no. 2, pp. 221-226, 1968.
- [67] T. J. Ulrych, "Application of Homomorphic Deconvolution to Seismology," *GEOPHYSICS*, vol. 36, no. 4, p. 650-660, 1971.
- [68] B.-Y. Liao, T.-W. Sheu, Y.-T. Yeh, H.-C. Huang and L.-S. Yang, "A Rupture Model for the 1999 Chi-Chi Earthquake from Inversion of Teleseismic Data Using the Hybrid Homomorphic Deconvolution Method," *Pure and Applied Geophysics*, vol. 170, no. 3, pp. 391-407, 2013.
- [69] M. Balbás and J. I. Díaz-Villafranca, "Application of Deconvolution to Blast Vibration Control," *Fragblast*, vol. 5, pp. 35-56, 2001.
- [70] R. Grüner and T. Taxt, "Cepstral estimation of arterial input functions in brain perfusion imaging," *Journal of Magnetic Resonance Imaging*, vol. 26, no. 3, p. 773-779, 2007.
- [71] T. G. J. Stockham, T. M. Cannon and R. B. Ingebretsen, "Blind deconvolution through digital signal processing," *Proceedings of the IEEE*, vol. 63, no. 4, pp. 678 - 692, 1975.
- [72] A. V. Oppenheim, "Superposition in a class of nonlinear systems," *Ph.D. dissertation, MIT*, May, 1964.
- [73] A. V. Oppenheim, R. W. Schafer and T. G. Stockham, "Nonlinear Filtering of Multiplied and Convolved Signals," *Proceedings of the IEEE*, vol. 56, no. 8, pp. 1264-1291, 1968.
- [74] A. V. Oppenheim and R. W. Schafer, in *Discrete-Time Signal Processing*, Upper Saddle River, NJ, Prentice-Hall, 1999, pp. 788-789.
- [75] A. V. Oppenheim and R. W. Schafer, "From frequency to quefrequency: a history of the cepstrum," *Signal Processing Magazine, IEEE*, vol. 21, no. 5, pp. 95-106, 2004.
- [76] C. Granger, "Investigating causal relations by econometric models and cross-spectral methods," *Econometrica*, vol. 37(3), pp. 424-438, 1969.
- [77] H. Akaike, "A new look at the statistical model identification," *Automatic Control, IEEE Transactions on*, vol. 19, no. 6, pp. 716 - 723, 1974.

- [78] G. Schwarz, "Estimating the Dimension of a Model," *The Annals of Statistics*, vol. 6, no. 2, pp. 461- 464, 1978.
- [79] G. Deshpande, K. Sathian and X. Hu, "Assessing and Compensating for Zero-lag Correlation Effects in Time-lagged Granger Causality Analysis of fMRI," *IEEE Transactions on Biomedical Engineering*, vol. 57, no. 6, p. 1446:1456, 2010.
- [80] M. Arnold, W. Miltner, H. Witte, R. Bauer and C. Braun, "Adaptive AR Modeling of Nonstationary Time Series by Means of Kalman Filtering," *IEEE TRANSACTIONS ON BIOMEDICAL ENGINEERING*, vol. 45, no. 5, pp. 553-562, 1998.
- [81] R. K. Kana and M. A. Just, "Autism as a disorder of functional brain connectivity," in *Handbook of Autism Spectrum Disorders*, D. G. Amaral, D. Geschwind and G. Dawson, Eds., New York, Oxford University Press, 2011, pp. 981-989.
- [82] R. K. Kana, L. E. Libero and M. S. Moore, "Disrupted cortical connectivity theory as an explanatory model for autism spectrum disorders," *Physics of life reviews*, vol. 8, no. 4, pp. 410-437, 2011.
- [83] R. K. Kana, L. E. Libero, C. P. Hu, H. D. Deshpande and J. S. Colburn, "Functional brain networks and white matter underlying theory-of-mind in autism," *Social Cognitive and Affective Neuroscience*, 2012.
- [84] G. Deshpande, Z. Li, P. Santhanam, C. D. Coles, M. E. Lynch, S. Hamann and X. Hu, "Recursive Cluster Elimination Based Support Vector Machine for Disease State Prediction Using Resting State Functional and Effective Brain Connectivity," *PLoS ONE*, vol. 5, no. 12, p. e14277, 2010.
- [85] M. Xia, J. Wang and Y. He, "BrainNet Viewer: A Network Visualizathion Tool for Human Brain Connectomics," *PLoS ONE*, vol. 8, no. 7, 2013.
- [86] M. M. Grant, C. Cannistraci, S. D. Hollon, J. Gore and R. Shelton, "Childhood trauma history differentiates amygdala response to sad faces within MDD," *Journal of Psychiatric Research*, vol. 45, no. 7, pp. 886-895, 2011.
- [87] M. T. Treadway, M. M. Grant, Z. Ding, S. D. Hollon, J. C. Gore and R. C. Shelton, "Early Adverse Events, HPA Activity and Rostral Anterior Cingulate Volume in MDD," *PLoS ONE*, vol. 4, no. 3, p. e4887, 2009.
- [88] J. P. Christianson, B. M. Thompson, L. R. Watkins and S. F. Maier, "Medial prefrontal cortical activation modulates the impact of controllable and uncontrollable stressor exposure on a social exploration test of anxiety in the rat," *Stress*, vol. 12, no. 5, pp. 445-450, 2009.
- [89] K. H. Wood, L. W. Ver Hoef and D. C. Knight, "Neural mechanisms underlying the conditioned diminution of the unconditioned fear response," *NeuroImage*, vol. 60, no. 1, pp. 787-799, 2012.
- [90] B. A. Eriksen and C. W. Eriksen, "Effects of noise letters upon identification of a target letter in a non- search task," *Perception & Psychophysics*, vol. 16, no. 1, pp. 143-149, 1974.
- [91] J. R. Sato, E. A. Junior, D. Y. Takahashi, M. de Maria Felix, M. J. Brammer and P. A. Morettin, "A method to produce evolving functional connectivity maps during the course of an fMRI experiment using wavelet-based time-varying Granger causality," *NeuroImage*, vol. 31, no. 1, pp. 187-196, 2006.

- [92] R. W. Cox, "AFNI: Software for Analysis and Visualization of Functional Magnetic," *Computers and Biomedical Research*, vol. 29, pp. 162-173, 1996.
- [93] A. Etkin, T. Egner and R. Kalisch, "Emotional processing in anterior cingulate and medial prefrontal cortex," *Trends in Cognitive Sciences*, vol. 15, no. 2, pp. 85-93, 2011.
- [94] K. N. Ochsner, R. D. Ray, J. C. Cooper, E. R. Robertson, S. Chopra, J. D. E. Gabrieli and J. J. Gross, "For better or for worse: neural systems supporting the cognitive down- and up-regulation of," *NeuroImage*, vol. 23, pp. 483-499, 2004.
- [95] R. Tandon, H. A. Nasrallah and M. S. Keshavan, "Schizophrenia, "just the facts" 4. Clinical features and conceptualization," *Schizophrenia Research*, vol. 110, pp. 1-23, 2009.
- [96] M. F. Green, "What are the functional consequences of neurocognitive deficits in schizophrenia?," *American Journal of Psychiatry*, vol. 153, no. 3, pp. 321-330, 1996.
- [97] P. F. Liddle, "Schizophrenic syndromes, cognitive performance and neurological dysfunction," *Psychological Medicine*, vol. 17, no. 1, pp. 49-57, 1987.
- [98] L. Deserno, P. Sterzer, T. Wüstenberg, A. Heinz and F. Schlagenhauf, "Reduced prefrontal-parietal effective connectivity and working memory deficits in schizophrenia," *The Journal of Neuroscience*, vol. 32, no. 1, pp. 12-20, 2012.
- [99] M. Bastian, S. Heyman and M. Jacomy, "Gephi: an open source software for exploring and manipulating networks," *International AAAI Conference on Weblogs and Social Media*, pp. 361-362, 2009.
- [100] F. Vinckier, L. Cohen, C. Oppenheim, A. Salvador, H. Picard, I. Amado, M. O. Krebs and R. Gaillard, "Reading impairment in schizophrenia: Dysconnectivity within the visual system," *Neuropsychologia*, vol. 53, pp. 187-196, 2014.
- [101] S. Walther, A. Federspiel, H. Horn, N. Razavi, R. Wiest, T. Dierks, W. Strik and T. J. Müller, "Alterations of white matter integrity related to motor activity in schizophrenia," *Neurobiology of Disease*, vol. 42, pp. 276-283, 2011.
- [102] S. Lacey, N. Tal, A. Amedi and K. Sathian, "A putative model of multisensory object representation," *Brain Topography*, vol. 21, no. 3-4, pp. 269-274, 2009.
- [103] S. Lacey, P. Flueckiger, R. Stilla, M. Lava and K. Sathian, "Object familiarity modulates the relationship between visual object imagery and haptic shape perception," *NeuroImage*, vol. 49, no. 3, pp. 1977-1990, 2010.
- [104] I. Ellison-Wright and E. Bullmore, "Anatomy of bipolar disorder and schizophrenia: a meta-analysis," *Schizophr. Res.*, vol. 117, p. 1-12, 2010.
- [105] J. Sui, G. Pearlson, A. Caprihan, T. Adali, K. A. Kiehl, J. Liu, J. Yamamoto and V. D. Calhoun, "Discriminating schizophrenia and bipolar disorder by fusing fMRI and DTI in a multimodal CCA+ joint ICA model," *NeuroImage*, vol. 57, p. 839-855, 2011.
- [106] N. Craddock and M. J. Owen, "The Kraepelinian dichotomy - going, going... but still not gone," *Br. J. Psychiatry*, vol. 196, pp. 92-95, 2010.
- [107] P. Lichtenstein, B. H. Yip, C. Björk, Y. Pawitan, T. D. Cannon, P. F. Sullivan and C. M. Hultman, "Common genetic determinants of schizophrenia and bipolar disorder in Swedish families: a population-based study," *Lancet*, vol. 373, p. 234-239, 2009.

- [108] A. Demjaha, J. H. MacCabe and R. M. Murray, "How Genes and Environmental Factors Determine the Different Neurodevelopmental Trajectories of Schizophrenia and Bipolar Disorder," *Schizophrenia Bulletin*, 2011.
- [109] R. M. Murray, P. Sham, J. Van Os, J. Zanelli, M. Cannon and C. McDonald, "A developmental model for similarities and dissimilarities between schizophrenia and bipolar disorder," *Schizophrenia Research*, vol. 71, no. 2-3, pp. 405-416, 2004.
- [110] T. A. Ketter, P. W. Wang, O. V. Becker, C. Nowakowska and Y. Yang, "Psychotic bipolar disorders: dimensionally similar to or categorically different from schizophrenia?," *J. Psychiatr. Res*, vol. 38, p. 47-61, 2004.